The Astrophysical Journal, 936:95 (17pp), 2022 September 10 https://doi.org/10.3847/1538-4357/ac886e

NuSTAR Observations of Intrinsically X-Ray Weak Quasar Candidates: An Obscuration-only Scenario

Chaojun Wang[1,2], B. Luo[1,2], W. N. Brandt[3,4,5], D. M. Alexander[6], F. E. Bauer[7,8,9], S. C. Gallagher[10], Jian Huang[1,2], Hezhen Liu[1,2], and D. Stern[11]

[1] School of Astronomy and Space Science, Nanjing University, Nanjing, Jiangsu 210093, People's Republic of China
[2] Key Laboratory of Modern Astronomy and Astrophysics (Nanjing University), Ministry of Education, Nanjing 210093, People's Republic of China
[3] Department of Astronomy & Astrophysics, 525 Davey Lab, The Pennsylvania State University, University Park, PA 16802, USA
[4] Institute for Gravitation and the Cosmos, The Pennsylvania State University, University Park, PA 16802, USA
[5] Department of Physics, 104 Davey Lab, The Pennsylvania State University, University Park, PA 16802, USA
[6] Centre for Extragalactic Astronomy, Department of Physics, Durham University, Durham DH1 3LE, UK
[7] Instituto de Astrofísica and Centro de Astroingeniería, Facultad de Física, Pontificia Universidad Católica de Chile, Casilla 306, Santiago 22, Chile
[8] Millennium Institute of Astrophysics, Nuncio Monseñor Sótero Sanz 100, Of 104, Providencia, Santiago, Chile
[9] Space Science Institute, 4750 Walnut Street, Suite 205, Boulder, CO 80301, USA
[10] Department of Physics & Astronomy and Institute for Earth and Space Exploration, The University of Western Ontario, London, ON N6A 3K7, Canada
[11] Jet Propulsion Laboratory, California Institute of Technology, 4800 Oak Grove Drive, MS 169-224, Pasadena, CA 91109, USA
Received 2022 April 6; revised 2022 August 8; accepted 2022 August 8; published 2022 September 6

Abstract

We utilize recent NuSTAR observations (co-added depth ≈55–120 ks) of PG 1001+054, PG 1254+047, and PHL 1811 to constrain their hard X-ray ($\gtrsim$5 keV) weakness and spectral shapes and thus to investigate the nature of their extreme X-ray weakness. These quasars showed very weak soft X-ray emission, and they were proposed to be intrinsically X-ray weak, with the X-ray coronae producing weak continuum emission relative to their optical/UV emission. However, the new observations suggest an alternative explanation. The NuSTAR 3–24 keV spectral shapes for PG 1001+054 and PHL 1811 are likely flat (effective power-law photon indices $\Gamma_{\rm eff} = 1.0^{+0.5}_{-0.6}$ and $\Gamma_{\rm eff} = 1.4^{+0.8}_{-0.7}$, respectively), while the shape is nominal for PG 1254+047 ($\Gamma_{\rm eff} = 1.8 \pm 0.3$). PG 1001+054 and PHL 1811 are significantly weak at hard X-ray energies (by factors of ≈26–74 at rest-frame 8 keV) compared to the expectations from their optical/UV emission, while PG 1254+047 is only hard X-ray weak by a factor of ≈3. We suggest that X-ray obscuration is present in all three quasars. We propose that, as an alternative to the intrinsic X-ray weakness + X-ray obscuration scenario, the soft and hard X-ray weakness of these quasars can be uniformly explained under an obscuration-only scenario. This model provides adequate descriptions of the multiepoch soft and hard X-ray data of these quasars, with variable column density and leaked fraction of the partial covering absorber. We suggest that the absorber is the clumpy dust-free wind launched from the accretion disk. These quasars probably have super-Eddington accretion rates that drive powerful and high-density winds.

Unified Astronomy Thesaurus concepts: Broad-absorption line quasar (183); X-ray quasars (1821); X-ray active galactic nuclei (2035); Accretion (14); Quasars (1319)

1. Introduction

Active galactic nuclei (AGNs) generally produce luminous X-ray emission, which is believed to originate largely from the accretion disk corona in the vicinity of the central supermassive black hole (SMBH) via inverse Compton scattering of the optical/UV seed photons from the accretion disk (e.g., Turner & Miller 2009; Done 2010; Gilfanov & Merloni 2014; Fabian et al. 2017). AGN X-ray continua typically have an intrinsic power-law shape ($N_E \propto E^{-\Gamma}$), and the mean value of the photon indices (Γ) for radio-quiet AGNs is around 1.9–2.0 with a scatter of ≈0.2 (e.g., Reeves et al. 1997; Just et al. 2007; Scott et al. 2011). Observations of the X-ray and UV emission from large samples of radio-quiet AGNs have revealed that the X-ray flux is closely correlated with the optical/UV flux, indicating a strong physical connection between the accretion disk and the X-ray corona. The correlation is typically expressed as a negative relation between the X-ray-to-optical power-law slope parameter ($\alpha_{\rm OX}$)[12] and the 2500 Å monochromatic luminosity ($L_{2500\ \text{Å}}$), and it is highly significant across a broad population of AGNs, ranging from moderate-luminosity AGNs to the most luminous quasars (e.g., Strateva et al. 2005; Steffen et al. 2006; Just et al. 2007; Lusso & Risaliti 2017; Liu et al. 2021).

The observed X-ray emission from AGNs may be modified by line-of-sight obscuration, resulting in lower observed X-ray fluxes than those expected from the $\alpha_{\rm OX}$–$L_{2500\ \text{Å}}$ relation. A common approach to parameterize the amount of X-ray weakness uses the $\Delta\alpha_{\rm OX}$ parameter, defined as the difference between the observed $\alpha_{\rm OX}$ value and the $\alpha_{\rm OX}$ value expected from the $\alpha_{\rm OX}$–$L_{2500\ \text{Å}}$ relation; $\Delta\alpha_{\rm OX} = -0.3838$ thus corresponds to a factor of X-ray weakness of 10 at rest-frame 2 keV. Type 2 AGNs are generally X-ray obscured, likely due to the dusty "torus" (e.g., Netzer 2015; Hickox & Alexander 2018). Type 1 AGNs may also have X-ray obscuration from largely dust-free gas.[13] For example, broad absorption line (BAL)

[12] $\alpha_{\rm OX}$ is defined as $\alpha_{\rm OX} = 0.3838\log(f_{2\ \rm keV}/f_{2500\ \text{Å}})$ (Tananbaum et al. 1979), where $f_{2\ \rm keV}$ and $f_{2500\ \text{Å}}$ are the rest-frame 2 keV and 2500 Å flux densities, respectively.
[13] Similar obscuration from dust-free gas might also be present in some of the type 2 AGNs, though usually not distinguishable from the torus obscuration.

quasars, which are characterized by blueshifted broad UV absorption lines (e.g., C IV λ1549), generally show weak X-ray emission (e.g., Gallagher et al. 2002, 2006; Fan et al. 2009; Gibson et al. 2009). One frequently adopted physical model for BAL quasars is the disk wind model, where the observed BALs originate from an outflowing equatorial wind launched from the accretion disk and radiatively driven by UV-line pressure (e.g., Murray et al. 1995; Proga et al. 2000; Matthews et al. 2016). This model usually invokes "shielding" gas between the wind and nucleus or a clumpy wind (e.g., Baskin et al. 2014; Matthews et al. 2016; Giustini & Proga 2019) to provide obscuration of the nuclear extreme-UV (EUV) and X-ray radiation, which might otherwise overionize the wind and hamper radiative acceleration. BAL quasars are considered generally to have larger inclination angles than non-BAL quasars, with the line of sight to the UV continuum region of the accretion disk intersecting the wind, leading to the observed BALs. The line of sight to the X-ray-emitting corona, though not necessarily the same as the UV line of sight, is likely also through the shielding gas or the clumpy wind, resulting in the often-observed X-ray weakness (e.g., Figure 1 of Luo et al. 2013). Besides BAL quasars, a small fraction ($5.8\% \pm 0.7\%$) of non-BAL type 1 quasars have been found to be X-ray weak, likely due to absorption (e.g., Pu et al. 2020). They may share a similar nature to the BAL quasars; they do not show any UV BALs, probably due to geometric effects (e.g., small inclination angles) or a low velocity of the wind along the UV line of sight (e.g., Giustini & Proga 2019).

A small subset of AGNs have been proposed to be intrinsically X-ray weak, producing much less X-ray emission than expected from the $\alpha_{\rm OX}$–$L_{2500\ \text{Å}}$ relation. These candidates are observed to be significantly X-ray weak with no clear evidence of X-ray obscuration. X-ray weakness caused by X-ray obscuration is usually identified from an X-ray spectral shape that is flatter than the intrinsic $\Gamma \approx 2$ power law, as soft X-ray photons are more heavily absorbed than hard X-ray photons. The effective power-law photon index ($\Gamma_{\rm eff}$) of an obscured spectrum should be smaller than 2; in the case of heavy absorption, the 0.5–5 keV $\Gamma_{\rm eff}$ can even reach a negative value. However, due to the frequent appearance of partial covering absorption in AGN X-ray spectra (e.g., Immler et al. 2003; Ricci et al. 2017; Leighly et al. 2019) with a small fraction of the intrinsic coronal emission leaking through the absorber, a soft X-ray ($\lesssim$5 keV) spectrum alone might be insufficient for identifying heavy ($N_{\rm H} \gtrsim 5 \times 10^{23}$ cm^{-2}) or Compton-thick ($N_{\rm H} > 1.5 \times 10^{24}$ cm^{-2}) X-ray obscuration, as the X-ray emission could be extremely weak (e.g., $\Delta\alpha_{\rm OX} < -0.3838$ or X-ray weakness factor of >10), yet the spectral shape is nominal with $\Gamma_{\rm eff} \approx 2$, dominated by the leaked component (see Section 4.2 for an illustration). On the other hand, the hard X-ray ($\gtrsim$5 keV) spectrum in this case should generally still be flat with $\Gamma_{\rm eff} \approx 0$–1, as the Compton-reflection component, from either the absorber or other reflectors (e.g., disk or torus), is expected to dominate (e.g., George & Fabian 1991; Comastri et al. 2011; Gandhi et al. 2014; Rovilos et al. 2014). It is based on these arguments that a small number of quasars have been proposed to be intrinsically X-ray weak; they are significantly X-ray weak, yet with nominal ($\Gamma_{\rm eff} \approx 2$) hard X-ray spectral shapes. The low-redshift ($z \lesssim 1$) candidates include a few BAL quasars that have NuSTAR observations (Luo et al. 2013, 2014), and the high-redshift ($z \approx 1.5$–3) candidates include a few Large Bright Quasar Survey (LBQS) BAL quasars with Chandra observations (Liu et al. 2018) and a few luminous quasars with XMM-Newton observations (Nardini et al. 2019). Given the significant X-ray weakness, the X-ray spectra of these candidates have very limited photon statistics, and thus the spectral shapes are poorly constrained and sometimes even rely on stacking analysis to obtain information on their average spectral properties (e.g., Luo et al. 2014).

One quasar that is considered a prototypical example of intrinsically X-ray weak quasars is PHL 1811, a non-BAL quasar at $z = 0.192$ (Leighly et al. 2007a). It is X-ray weak by a factor of ≈40–130 with a steep 0.3–5 keV XMM-Newton spectrum ($\Gamma \approx 2.3$). There are no published hard X-ray constraints, but its fast X-ray variability (flux varying by a factor of ≈4 in 12 days) argues against a heavily obscured spectrum dominated by distant reflection/scattering (Leighly et al. 2007a, 2007b). PHL 1811 has distinctive UV emission-line properties, including a small C IV rest-frame equivalent width (REW), a large C IV blueshift, and strong UV Fe II and Fe III emission. Luo et al. (2015) conducted a systematic survey of the X-ray properties of PHL 1811 analogs, a sample of high-redshift quasars selected with UV emission-line properties similar to those of PHL 1811. This sample of 18 PHL 1811 analogs turned out to be almost exclusively (17/18; 94%) X-ray weak, by an average X-ray weakness factor of 39. However, unlike PHL 1811 itself, many of these PHL 1811 analogs appear to be X-ray obscured, as the sample-stacked effective photon index ($\Gamma_{\rm eff} = 1.16^{+0.37}_{-0.32}$) indicates a flat spectral shape on average. Luo et al. (2015) speculated that Occam's razor would favor a uniform explanation for the X-ray weakness of all these objects and that perhaps hard X-ray data of PHL 1811 would reveal a highly obscured component.

In this paper, we present improved hard X-ray constraints from deeper NuSTAR observations of two low-redshift, intrinsically X-ray weak quasar candidates in Luo et al. (2014), PG 1001+054 (hereafter PG 1001) and PG 1254+047 (hereafter PG 1254). We also provide for the first time hard X-ray constraints for PHL 1811 using archival NuSTAR and XMM-Newton observations. Based on the results, we suggest that X-ray obscuration is present in all three quasars, and we propose that intrinsic X-ray weakness is not required to explain the X-ray weakness of these objects. The NuSTAR, Chandra, and XMM-Newton data of these quasars can be uniformly explained with an obscuration scenario where the partial covering absorber has variable column density and leaked fraction (partial covering fraction). The paper is organized as follows. We describe the soft and hard X-ray observations and data analyses in Section 2. We present X-ray and multi-wavelength properties of the three quasars in Section 3. In Section 4, we propose that these quasars are likely X-ray obscured and describe how an obscuration scenario may explain their soft and hard X-ray weakness, without invoking intrinsic X-ray weakness. The absorber is likely the clumpy dust-free wind launched from the accretion disk. We summarize in Section 5. In the Appendix, we present new hard X-ray constraints from a recent XMM-Newton observation of LBQS 1442 − 0011, a high-redshift, intrinsically X-ray weak quasar candidate in Liu et al. (2018); the results are consistent with our proposed obscuration scenario.

Throughout this paper, we use a cosmology with $H_0 = 67.4$ km s^{-1} Mpc^{-1}, $\Omega_M = 0.315$, and $\Omega_\Lambda = 0.685$ (Planck Collaboration et al. 2020). Uncertainties are quoted at a 1σ

Table 1
Basic Object Properties and List of Observations

Object Name	z	m_B	$\log M_{\rm BH}$ ($M_\odot$)	$L/L_{\rm Edd}$	$\log L_{2500\,\text{Å}}$ (erg s^{-1} Hz^{-1})	$N_{\rm H,Gal}$ (10^{20} cm^{-2})	Observatory	Observation ID	Obs. Date	Exp (ks)
(1)	(2)	(3)	(4)	(5)	(6)	(7)	(8)	(9)	(10)	(11)
PG 1001+054	0.161	16.1	7.74	0.5	29.9	2.38	XMM-Newton	0150610101	2003 May 4	8.6
							Chandra	11852	2010 Jan 11	4.9
							NuSTAR	60001122002	2013 Jun 28	19.6
							NuSTAR	60501014001	2020 May 23	101.1
PG 1254+047	1.026	15.8	9.68	0.3	31.5	2.03	Chandra	832	2000 May 29	36.0
							NuSTAR	60001123002	2013 Jun 27	29.4
							NuSTAR	60401013002	2019 Jun 8	88.0
PHL 1811	0.192	13.9	8.25	1.6	30.9	4.22	Chandra	2975	2001 Dec 5	9.3
							Chandra	2985	2001 Dec 17	9.8
							XMM-Newton	0204310101	2004 Nov 1	23.5
							XMM-Newton	0761910201	2015 Nov 29	39.9
							NuSTAR	60101004002	2015 Nov 28	54.7

Note. Columns (1) and (2): object name and redshift. Column (3): B-band magnitude. Columns (4) and (5): single-epoch virial BH mass and Eddington ratio from Shen et al. (2011) (for PG 1001 and PG 1254) or Leighly et al. (2007a) (for PHL 1811). Column (6): 2500 Å monochromatic luminosity from Shen et al. (2011) (for PG 1001 and PG 1254) or Leighly et al. (2007a) (for PHL 1811). Column (7): Galactic neutral hydrogen column density (HI4PI Collaboration et al. 2016). Columns (8) and (9): observatory and observation ID. Column (10): observation start date. Column (11): cleaned exposure time; for NuSTAR observations, it is the average value of the FPMA and FPMB exposure times.

confidence level, and limits are at a 90% confidence level. The energy ranges used in our photometric and spectroscopic analyses are 0.3–8 keV for Chandra observations, 0.3–10 keV for XMM-Newton observations, and 3–24 keV for NuSTAR observations, unless otherwise specified. Due to the X-ray weakness of the three quasars, all X-ray spectra were grouped with at least 1 count per bin, and the W statistic[14] of XSPEC (v12.10.1; Arnaud 1996) was used in spectral fitting. Galactic absorption (HI4PI Collaboration et al. 2016) was included in the X-ray spectral modeling.

2. Object Properties, X-Ray Observations, and X-Ray Data Analyses

2.1. Basic Object Properties

The basic properties of the three quasars are listed in Table 1. PG 1001 is at $z = 0.161$ with a B-band magnitude of 16.1. Its Hβ-based single-epoch virial SMBH mass ($M_{\rm BH}$) is $\approx 5.5 \times 10^7\ M_\odot$, and the estimated Eddington ratio is ≈0.5 (Shen et al. 2011). The FWHM of its Hβ emission line is 1740 km s^{-1}, and thus it was classified as a narrow-line type 1 quasar (NLQ1; Wills et al. 2000), which refers to type 1 quasars with narrow (FWHM < 2000 km s^{-1}) Hβ emission lines (e.g., footnote 1 of Wills et al. 2000). It also shows weaker [O III] λ5007 emission compared to typical quasars (REW smaller by a factor of ≈2; Vanden Berk et al. 2001; Shen et al. 2011).

PG 1254 is a luminous quasar at $z = 1.026$ with a B-band magnitude of 15.8. The Mg II-based single-epoch virial SMBH mass is $\approx 4.8 \times 10^9\ M_\odot$, and the estimated Eddington ratio is ≈0.3 (Shen et al. 2011). There are no Hβ or [O III] measurements available in the literature.

PHL 1811, at $z = 0.192$, is very bright with a B-band magnitude of 13.9. Its Hβ-based single-epoch virial SMBH mass is $\approx 1.8 \times 10^8\ M_\odot$, and its estimated Eddington ratio is ≈1.6 (Leighly et al. 2007a). We caution that the virial SMBH mass and the estimated Eddington ratio are subject to large uncertainties, especially in the super-Eddington regime, as the virialization assumption may no longer be valid when the broad emission line region (BELR) is likely exposed to large and anisotropic radiation pressure (e.g., Marconi et al. 2008, 2009; Netzer & Marziani 2010). PHL 1811 was classified as an NLQ1 with no apparent [O III] λ5007 emission (Leighly et al. 2007b).

2.2. NuSTAR Observations and Data Analysis

PG 1001 and PG 1254 were observed by NuSTAR in 2013 with cleaned exposure times of 19.6 and 29.4 ks, respectively. They were not detected in the 8–24 keV band individually, but they were considered good candidates for intrinsically X-ray weak quasars from X-ray stacking analysis (Luo et al. 2014). We obtained much deeper NuSTAR observations of PG 1254 in 2019 and PG 1001 in 2020 with exposure times of ≈100 ks (PI: W. N. Brandt), with the aim of detecting them individually in the 8–24 keV band and providing improved spectral shape constraints. PHL 1811 has an archival NuSTAR observation in 2015 with a cleaned exposure time of 54.7 ks, simultaneous to a 39.9 ks XMM-Newton observation (PI: K. Leighly). The details of the NuSTAR observations are listed in Table 1.

For NuSTAR data reduction, we used HEASoft (v6.29) and the NuSTAR Data Analysis Software (NuSTARDAS; v2.1.1) with NuSTAR CALDB 20210728. We used the NUPIPELINE script to generate calibrated clean event files from the unfiltered event files of the two focal plane module detectors (FPMA and FPMB). For the 2019 NuSTAR observation of PG 1254, background event rates were slightly elevated around the South Atlantic Anomaly (SAA), and we followed the recommendations from the NuSTAR instrument team and applied an additional SAA filter (SAAMODE = OPTIMIZED, TENTABLE = YES, and SAACALC = 1) during the NUPIPELINE processing. We created NuSTAR images using the Chandra Interactive Analysis of Observation (CIAO; v4.13)[15] tool DMCOPY in three energy bands: 3–24 keV (full band), 3–8 keV (soft band), and 8–24 keV (hard band).

For each NuSTAR observation, we co-added the FPMA and FPMB images to improve sensitivity, which helps in detecting

[14] https://heasarc.gsfc.nasa.gov/docs/xanadu/xspec/manual/XSappendixStatistics.html

[15] http://cxc.harvard.edu/ciao/

and characterizing faint NuSTAR sources (e.g., Lansbury et al. 2017). The co-added images were created by combining the FPMA and FPMB images in each of the three bands using the HEAsoft tool XIMAGE. These images were then used for source detection and aperture photometry. For each co-added image, we searched for X-ray sources using the CIAO tool WAVDETECT (Freeman et al. 2002) with a false-positive probability threshold of 10^{-5} and wavelet scales of 2, 2.83, 4, 5.66, 8, 11.31, and 16 pixels (e.g., Luo et al. 2014); the NuSTAR pixel size is 2.46″. In the 2013 observations, PG 1001 and PG 1254 were detected in the soft and full bands but not in the hard band. They were detected in all three bands in the latest deeper observations. PHL 1811 was also detected in all three bands. In the following analysis, we adopted the full-band WAVDETECT positions as the X-ray positions. The offsets between the X-ray and optical positions range from 3.4″ to 9.4″, which are typical for faint NuSTAR sources (e.g., Lansbury et al. 2017).

We extracted source and background spectra using the NUPIPELINE script. We used 35″-radius circular source regions centered on the X-ray positions and annular background regions centered on the X-ray positions with inner radii of 120″ and outer radii of 180″. We verified that there are no sources in the background regions. For each observation, we merged the FPMA and FPMB source spectra, background spectra, and response files using the HEASoft tool ADDSPEC.

2.3. Archival Chandra and XMM-Newton Observations and Data Analyses

The archival Chandra and XMM-Newton observations of the three quasars are listed in Table 1.[16] For Chandra data reduction, we used the CIAO CHANDRA_REPRO script to generate new level 2 event files. Background flares were then filtered with the DEFLARE script using an iterative 3σ clipping algorithm. We created 0.5–8 keV images from the cleaned event files using DMCOPY. We searched for X-ray sources in the X-ray images using WAVDETECT with a false-positive probability threshold of 10^{-6} and wavelet scales of 1, 1.414, 2, 2.828, 4, 5.656, and 8 pixels. The three quasars were all detected within 0.″22–0.″42 of the optical positions. For each observation, the source spectrum was extracted using the SPECEXTRACT tool from a circular region centered on the X-ray position with a radius of 2″. The background spectrum was extracted from an annular region centered on the X-ray position with an inner radius of 6″ and an outer radius of 10″; we verified that the background regions do not contain any X-ray sources.

For the XMM-Newton observations, we used only the data from the pn camera.[17] We used the Science Analysis System (SAS; v1.2) to process the data, following the standard procedure described in the SAS Data Analysis Threads.[18] We used the EPPROC tool to produce calibrated event files. A threshold of 0.4 counts s^{-1} was adopted to filter background flares. We created good-time-interval files using the TABGTIGEN script, and we generated cleaned event files using the EVSELECT tool. For each observation, we used the EVSELECT tool to extract source and background spectra, with a 30″-radius circular source region centered on the optical position of the quasar and a 80″-radius circular, source-free background region on the same CCD chip as the source region.

For the 2015 XMM-Newton observation of PHL 1811, we also used the Optical Monitor (OM) photometric data for constructing its spectral energy distribution (SED).[19] We generated nine exposures for the five filters (UVW2, UVM2, UVW1, *U*, *B*) using the OMICHAIN script, and the photometric measurements of every exposure were recorded in the SWSRLI files. We extracted the magnitude measurements from these files and adopted the mean magnitude for each filter. The coincidence loss corrections (due to the high count rates) were applied during the pipeline processing.

3. X-Ray and Multiwavelength Properties

3.1. Soft X-Ray Weakness and Obscuration Signatures from Archival X-Ray Observations

3.1.1. PG 1001

PG 1001 was observed by XMM-Newton and Chandra in 2003 and 2010 with exposure times of 8.6 and 4.9 ks, respectively, and the results were presented in Schartel et al. (2005) and Saez et al. (2012). As described in Section 2.3, we reduced these data and extracted the corresponding X-ray spectra. We performed simple power-law spectral fitting of the 2003 XMM-Newton spectrum in the 1–10 keV band and the 2010 Chandra spectrum in the 1–8 keV band; a lower energy bound of 1 keV was adopted here because there is apparent soft X-ray excess emission in the 0.3–1 keV XMM-Newton spectrum that is probably related to ionized absorption (Schartel et al. 2005). The resulting power-law photon indices are 0.8 ± 0.2 and $1.3^{+1.1}_{-1.0}$, indicative of X-ray obscuration. From the best-fit results, we derived two $\alpha_{\rm OX}$ values for PG 1001, and they are shown in the $\alpha_{\rm OX}$ versus $L_{2500\ \text{Å}}$ plane in Figure 1; the $L_{2500\ \text{Å}}$ measurement is from Shen et al. (2011). Besides the soft X-ray weakness, there is also X-ray flux variability between these two observations. We then computed the $\Delta\alpha_{\rm OX}$ parameters, which are -0.58 ± 0.15 for the XMM-Newton observation and -0.75 ± 0.16 for the Chandra observation, corresponding to X-ray weakness factors of 32^{+47}_{-19} and 88^{+144}_{-55} at rest-frame 2 keV, respectively. The $\Delta\alpha_{\rm OX}$ uncertainties were dominated by the $\alpha_{\rm OX}$ rms scatter (≈0.15; Table 5 of Steffen et al. 2006) of the $\alpha_{\rm OX}$–$L_{2500\ \text{Å}}$ relation. We note that there does not appear to be any strong long-term UV/optical variability of the three quasars in our study (maximum flux variability amplitudes ≈16%–80%; see Section 3.3), and thus the large X-ray weakness factors derived using nonsimultaneous X-ray and UV/optical data are not significantly affected by any UV/optical variability.

3.1.2. PG 1254

PG 1254 has a 36.0 ks Chandra observation in 2000 that was studied in Sabra & Hamann (2001). We performed simple power-law spectral fitting of this Chandra spectrum, and the resulting photon index is 0.6 ± 0.3, indicative of X-ray

[16] PHL 1811 has another Chandra observation in 2012 with an exposure time of 2.0 ks (see footnote 18 of Luo et al. 2015); we do not use this short observation in the present study, as it does not have sufficient statistics to place meaningful constraints on relevant parameters.

[17] We have checked the MOS data, which have lower photon statistics, especially in the 5–10 keV band that is of interest to this study; combining the pn spectra with the low signal-to-noise ratio MOS spectra might introduce additional systematic uncertainties.

[18] http://www.cosmos.esa.int/web/xmm-newton/sas-threads

[19] The 2004 OM observation of PHL 1811 used only one filter, and its photometric measurement does not suggest any variability compared to the 2015 OM results.

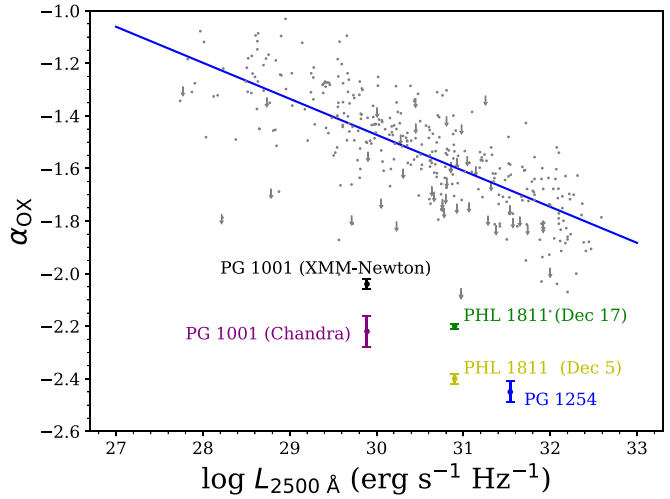

Figure 1. X-ray-to-optical power-law slope parameter (α_{OX}) vs. 2500 Å monochromatic luminosity for the three quasars, showing their significant soft X-ray weakness derived using archival Chandra and XMM-Newton observations. For PHL 1811, the α_{OX} values from the 2001 December 5 and December 17 Chandra observations are shown; the α_{OX} measurements from the two XMM-Newton observations not shown here are very close to the 2001 December 5 Chandra value. The solid blue line represents the α_{OX}–$L_{2500\,Å}$ relation from Steffen et al. (2006). The small gray circles and downward-pointing arrows represent the α_{OX} values and upper limits of the Steffen et al. (2006) AGN sample, respectively.

obscuration. Its location in the α_{OX} versus $L_{2500\,Å}$ plane is shown in Figure 1; the $L_{2500\,Å}$ measurement is from Shen et al. (2011). The corresponding $\Delta\alpha_{OX}$ value is -0.74 ± 0.16, indicating an X-ray weakness factor of 87^{+139}_{-53} at rest-frame 2 keV.

3.1.3. PHL 1811

PHL 1811 has two Chandra observations and two XMM-Newton observations, as listed in Table 1; the first three were presented in Leighly et al. (2007a). From simple power-law spectral fitting of the two Chandra and two XMM-Newton spectra, we obtained steep spectral shapes with photon indices in the range of ≈2.0–2.6, consistent with those in Leighly et al. (2007a). The two α_{OX} values from the 2001 December 5 and December 17 Chandra observations are shown in Figure 1, using the $L_{2500\,Å}$ value adopted from Leighly et al. (2007a). The $\Delta\alpha_{OX}$ values are -0.78 ± 0.15 for the December 5 observation and -0.58 ± 0.15 for the December 17 observation, corresponding to X-ray weakness factors of 108^{+160}_{-64} and 33^{+48}_{-20} at rest-frame 2 keV, respectively. We do not show the α_{OX} values from the two XMM-Newton observations in Figure 1, as they are very close to the 2001 December 5 Chandra value (e.g., $\Delta\alpha_{OX} = -0.81$ for the 2015 XMM-Newton observation).

In summary, previous soft X-ray observations of the three quasars have revealed significant soft X-ray weakness, with the rest-frame 2 keV fluxes ≈32–108 times weaker compared to the expectations from their optical/UV emission. The soft X-ray spectra of PG 1001 and PG 1254 have flat spectral shapes, indicative of X-ray obscuration, while the soft X-ray spectra of PHL 1811 do not show evidence for X-ray obscuration.

3.2. Hard X-Ray Weakness and Spectral Shape Constraints from NuSTAR

For each NuSTAR observation, we performed aperture photometry using the co-added FPMA + FPMB images in the three bands (soft, hard, and full). In each image, we extracted source counts (S) and background counts (B) from the same source and background regions used in the spectral extraction in Section 2.2. The encircled-energy fraction of the source region is 63.9% according to the NuSTAR point-spread function. We determined the source significance by calculating the binomial no-source probability (P_B; e.g., Luo et al. 2013), which is defined as

$$P_B(X \geqslant S) = \sum_{X=S}^{N} \frac{N!}{X!(N-X)!} p^X (1-p)^{N-X}. \quad (1)$$

In this expression, $N = S + B$ and $p = 1/(1 + BACKSCAL)$, where $BACKSCAL$ is the ratio between the exposure-time-weighted areas of the background and source regions. A smaller P_B value indicates a more significant signal. We considered the source detected in a band if the measured P_B value is smaller than 0.01 (corresponding to a $>2.6\sigma$ significance level). With this criterion, PG 1001 and PG 1254 were not detected in the hard band in their 2013 observations, and the three quasars were detected in all the other images; these results are consistent with the WAVDETECT results in Section 2.2. In the hard band, the P_B values for PG 1001 and PG 1254 in their latest observations are 5.4×10^{-7} (5.0σ) and 3.8×10^{-6} (4.6σ), respectively, and P_B is 1.1×10^{-3} (3.3σ) for PHL 1811; these values indicate significant detections in the hard band. The NuSTAR hard-band images of the three quasars are displayed in Figure 2.

For the detected sources, we computed their aperture-corrected net counts $(S - B/BACKSCAL)/0.639$. The associated errors were derived from the 1σ Poisson errors of the extracted source and background counts (Gehrels 1986). Compared to PG 1001 and PG 1254, PHL 1811 has larger relative count errors in the hard band, consistent with its larger hard-band P_B value (lower detection significance). For undetected sources, we calculated 90% confidence level upper limits on the source counts following the Bayesian approach of Kraft et al. (1991). The net counts and upper limits in the three bands are listed in Table 2.

For each quasar in each observation, we derived an effective power-law photon index (Γ_{eff}) from the band ratio, which is the ratio between the hard-band (8–24 keV) and soft-band (3–8 keV) counts, based on the following procedure: (1) For a given set of Γ values, we produced a set of mock power-law spectra using the XSPEC FAKEIT routine and the spectral response files. (2) For each mock spectrum, we computed the corresponding band ratio. (3) We interpolated the Γ versus band ratio set to derive the Γ_{eff} value from the measured band ratio. The Γ_{eff} values are listed in Table 2. The 1σ errors on Γ_{eff} were propagated from the errors of the band ratios derived using BEHR (Park et al. 2006). If the quasar was not detected in the hard band, we computed the lower limit on Γ_{eff} from the upper limit on the band ratio calculated using BEHR. In this case, $\Gamma_{eff} = 2.0$ was adopted in the following calculations of fluxes, flux densities, and luminosities; we consider this more appropriate than using the lower limit value, and adopting a value different from 2.0 would not affect the results significantly.

To compute fluxes, we obtained conversion factors from count rates to fluxes in the three bands using the mock spectrum with a photon index of Γ_{eff}. Flux errors were propagated from the count errors, and flux upper limits were

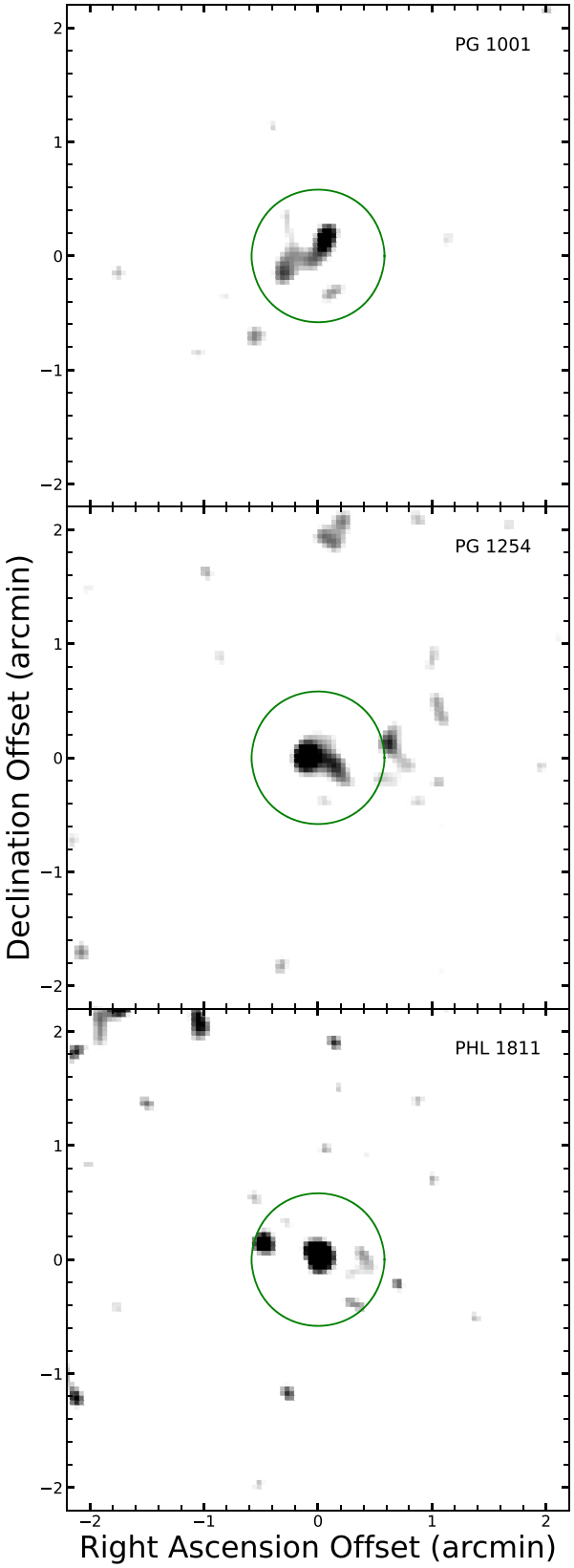

Figure 2. NuSTAR hard-band (8–24 keV) images of the three quasars, smoothed with a Gaussian kernel with standard deviation of 2.0 pixels. Each image is centered on the corresponding X-ray source position, and the circle indicates the 35″-radius aperture used for source extraction. Due to statistical fluctuations, the smoothed images of these faint sources do not have circular morphologies following the NuSTAR on-axis point-spread function.

derived from the upper limits on the net counts. The luminosity in the rest-frame 2–10 keV band (L_X) in each observation was derived from the full-band flux adopting a power-law spectrum with a photon index of $\Gamma_{\rm eff}$. The X-ray fluxes and luminosities are listed in Table 2. For PG 1001 and PG 1254 that have two NuSTAR observations, the photometric properties from the two observations are overall consistent within the errors, except for the $\Gamma_{\rm eff}$ constraints of PG 1001, which suggest possible spectral shape evolution. We stacked their photometric measurements to derive average properties; the results are also listed in Table 2.

We calculated the factor of X-ray weakness at rest-frame 8 keV (f_w), which is defined as the ratio between the expected and observed 8 keV flux density ($f_w = f_{\nu,\rm expected}/f_{\nu,\rm observed}$). The observed 8 keV flux density was computed from the full-band flux for a power-law spectrum with a photon index of $\Gamma_{\rm eff}$, and the expected 8 keV flux density was calculated from the Steffen et al. (2006) $\alpha_{\rm OX}$–$L_{2500\,\text{Å}}$ relation adopting a $\Gamma = 2$ power-law spectrum. The f_w uncertainties were propagated from the $\alpha_{\rm OX}$ rms scatter of the $\alpha_{\rm OX}$–$L_{2500\,\text{Å}}$ relation. We caution that f_w is different from the factor of X-ray weakness quantified by the $\Delta\alpha_{\rm OX}$ parameter (Section 1), which is for rest-frame 2 keV.

Compared to the previous hard-band nondetections, the deeper NuSTAR observations of PG 1001 and PG 1254 improve the source detection significance and provide better constraints on the hard X-ray weakness factors and hard X-ray spectral shapes. The NuSTAR observation of PHL 1811 provides first-ever hard X-ray constraints for this extreme quasar. PG 1001 and PHL 1811 are significantly hard X-ray weak ($f_w \approx 26$–74), while PG 1254 is only X-ray weak by a factor of $\approx$2.7 in the hard X-rays despite its significant soft X-ray weakness (Figure 1). Although the 2013 observation of PG 1001 suggests a potentially typical hard X-ray spectral shape ($\Gamma_{\rm eff} > 1.5$), the 2020 observation and the 2013+2020 stacked data suggest flat spectral shapes ($\Gamma_{\rm eff} \approx 0.4$–$1.0$). Both observations of PG 1254 suggest nominal spectral shapes with $\Gamma_{\rm eff} \approx 1.8$. The PHL 1811 observation surprisingly reveals that its hard X-ray photon index ($\Gamma_{\rm eff} = 1.4^{+0.8}_{-0.7}$), though loosely constrained, appears marginally smaller than its soft X-ray (0.3–5 keV) photon index (2.3 ± 0.1) from the 2004 XMM-Newton observation (Leighly et al. 2007a).

3.3. Spectral Energy Distributions and Optical/Infrared Variability

We constructed infrared (IR) to X-ray SEDs for the three quasars. We collected IR–UV photometric data from the Wide-field Infrared Survey Explorer (WISE; Wright et al. 2010), Near-Earth Object WISE (NEOWISE; Mainzer et al. 2014), Two Micron All Sky Survey (2MASS; Skrutskie et al. 2006), Sloan Digital Sky Survey (SDSS; York 2000), and Galaxy Evolution Explorer (GALEX; Martin et al. 2005) catalogs. For the two PG quasars, we also included their SED data from Neugebauer et al. (1987). We added Spitzer photometric measurements for PG 1001 (Veilleux et al. 2009). For PHL 1811, we included the 2001 Hubble Space Telescope/Space Telescope Imaging Spectrograph UV spectrum and the 2015 XMM-Newton OM measurements. The optical and UV data have been corrected for Galactic extinction following the dereddening approach in Cardelli et al. (1989) and O'Donnell

Table 2
NuSTAR Photometric Properties

Object Name	Obs. Year	Net Source Counts[a]			$\Gamma_{\rm eff}$[b]	Flux (10^{-14} erg cm^{-2} s^{-1})			log $L_{\rm X}$ (erg s^{-1})	f_w[c]
		3–24 keV	3–8 keV	8–24 keV		3–24 keV	3–8 keV	8–24 keV	2–10 keV	
PG 1001	2013	52^{+16}_{-15}	40^{+13}_{-11}	<26	>1.5 (2.0)	$7.8^{+2.4}_{-2.2}$	$4.4^{+1.2}_{-1.4}$	<5.9	42.7	16^{+24}_{-10}
PG 1001	2020	172^{+35}_{-34}	57^{+24}_{-23}	113^{+27}_{-25}	$0.4^{+0.6}_{-0.9}$	$7.8^{+1.6}_{-1.5}$	$1.1^{+0.5}_{-0.4}$	$6.6^{+1.6}_{-1.5}$	42.0	34^{+50}_{-20}
PG 1001	2013+2020	223^{+38}_{-37}	98^{+26}_{-25}	125^{+29}_{-27}	$1.0^{+0.5}_{-0.6}$	7.2 ± 1.2	$1.7^{+0.5}_{-0.4}$	$5.5^{+1.3}_{-1.2}$	42.2	26^{+38}_{-15}
PG 1254	2013	63^{+21}_{-19}	35^{+15}_{-14}	<50	>0.4 (2.0)	$6.2^{+2.0}_{-1.9}$	$2.5^{+1.1}_{-1.0}$	<7.3	44.5	$3.4^{+5.0}_{-2.0}$
PG 1254	2019	275^{+38}_{-36}	171^{+28}_{-26}	104^{+27}_{-25}	$1.8^{+0.5}_{-0.4}$	$10.0^{+1.4}_{-1.3}$	4.3 ± 0.7	$5.7^{+1.5}_{-1.4}$	44.5	$2.5^{+3.6}_{-1.5}$
PG 1254	2013+2019	338^{+43}_{-41}	206^{+31}_{-30}	132^{+30}_{-29}	1.8 ± 0.3	$9.1^{+1.2}_{-1.1}$	3.8 ± 0.6	5.3 ± 1.2	44.5	$2.7^{+3.9}_{-1.6}$
PHL 1811	2015	113^{+28}_{-26}	59^{+20}_{-18}	55^{+21}_{-19}	$1.4^{+0.8}_{-0.7}$	$7.0^{+1.7}_{-1.6}$	$2.2^{+0.8}_{-0.7}$	$4.9^{+1.8}_{-1.7}$	42.6	74^{+109}_{-44}

Notes.
[a] The errors were derived from the 1σ errors of the extracted source and background counts (Gehrels 1986). For undetected sources, we calculated 90% confidence level upper limits on the source counts following the Bayesian approach of Kraft et al. (1991).
[b] Effective power-law photon index. If the source is not detected in the 8–24 keV band, a lower limit value is provided, but $\Gamma_{\rm eff} = 2.0$ (as shown in parentheses) was adopted in calculating the fluxes, flux densities, and luminosity.
[c] Factor of X-ray weakness at rest-frame 8 keV, derived by comparing the observed 8 keV flux density to that expected from the Steffen et al. (2006) $\alpha_{\rm OX}$–$L_{2500\ \text{Å}}$ relation assuming a $\Gamma = 2$ power-law spectrum. The uncertainty is dominated by the scatter of the $\alpha_{\rm OX}$–$L_{2500\ \text{Å}}$ relation.

(1994). The SEDs are shown in Figure 3. For comparison, we also plotted in each panel the mean SED of high-luminosity radio-quiet quasars in Krawczyk et al. (2013) normalized to the 2500 Å luminosity. The X-ray component of the mean quasar SED is a $\Gamma = 2$ power-law continuum that follows the $\alpha_{\rm OX}$–$L_{2500\ \text{Å}}$ relation. The IR-to-UV SEDs of the three quasars are broadly consistent with those of typical quasars; the slight deviations in the IR for PG 1001 and PHL 1811 are within the scatters (≈0.2–0.25 dex) of the mean quasar SED at these frequencies.

We added soft and hard X-ray measurements to the SEDs. We used the 2 keV luminosities from the power-law spectral fitting of the Chandra or XMM-Newton spectra (Section 3.1). From the NuSTAR full-band fluxes (Section 3.2; stacked results were used for PG 1001 and PG 1254), we derived 8 and 15 keV luminosities adopting power-law spectra with the measured $\Gamma_{\rm eff}$ values. Compared to the typical quasar SED, which follows the $\alpha_{\rm OX}$–$L_{2500\ \text{Å}}$ relation, the soft and hard X-ray weakness of the three quasars is evident. For PHL 1811, we also show the soft X-ray spectral slopes from the two XMM-Newton observations and the hard X-ray spectral slope constrained from the NuSTAR observation. The spectral slopes differ beyond the 1σ level, suggesting that X-ray obscuration might also be present in PHL 1811. The SEDs of the three quasars also show clearly that they deviate from the observed $L_{\rm X}$–$L_{\rm MIR}$ relations for typical quasars (e.g., Lutz et al. 2004; Mateos et al. 2015; Stern 2015; Chen et al. 2017; Martocchia et al. 2017), with $L_{\rm MIR}$ being the mid-IR luminosity measured at rest-frame 6 μm. The offsets from the relations are approximately quantified by the f_w values (Table 2), and PHL 1811 is ≈70 times X-ray underluminous compared to its mid-IR luminosity. Integrating the IR-to-X-ray SEDs, we estimate the bolometric luminosities to be 3.4×10^{45} erg s^{-1} for PG 1001, 2.1×10^{47} erg s^{-1} for PG 1254, and 4.2×10^{46} erg s^{-1} for PHL 1811. These values are consistent with those provided in Shen et al. (2011) and Leighly et al. (2007a).

The IR-to-UV SED data are not simultaneous and may be affected by variability. Mild variability is apparent in the SED of PG 1001, where the more recent optical and near-IR measurements are ≈2%–60% lower than the Neugebauer et al. (1987) data. To investigate the optical variability of these three quasars, we further examined their long-term optical light curves constructed using the public catalogs of the Zwicky Transient Facility Data Release 9 (ZTF DR9; Bellm & Kulkarni et al. 2019) and the Catalina Real-Time Transient Survey (CRTS; Drake et al. 2009). The maximum flux variability amplitudes in the ZTF g band range from 13% to 40%, and in the CRTS V band they range from 16% to 80%; PG 1001 varied the most among the three quasars. Since PG 1001 has the strongest optical variability, we also checked its IR light curve from the NEOWISE catalog. Between 2014 May and 2020 November, its maximum flux variability amplitude in the W1 (W2) band is 18% (13%). The mild optical/IR variability observed in these quasars suggests that the overall accretion power did not change significantly (e.g., by factors of >2) over the years. Compared to the soft and hard X-ray weakness factors ($\Delta\alpha_{\rm OX}$ and f_w in Sections 3.1 and 3.2), the UV/optical variability factors are much smaller, indicating that the X-ray weakness factors assessed using nonsimultaneous UV/optical data are not heavily biased.

4. Discussion

The three quasars in this study were considered among the best candidates for intrinsically X-ray weak quasars, with coronae that produce weaker X-ray emission than expected from the $\alpha_{\rm OX}$–$L_{2500\ \text{Å}}$ relation. Intrinsic X-ray weakness and X-ray obscuration are not mutually exclusive. In fact, at least for PG 1001 and PG 1254, the presence of X-ray obscuration is clearly indicated by their flat spectral shapes in the soft X-rays (Section 3.1). Therefore, it was proposed in Luo et al. (2014) that the Chandra, XMM-Newton, and NuSTAR data of PG 1001 and PG 1254 could be explained by intrinsically weak X-ray continua modified by Compton-thin absorption. In the subsections below, we first suggest that X-ray obscuration is also present in PHL 1811 given the hard X-ray constraints. We then propose that, as an alternative to the intrinsic X-ray weakness + X-ray obscuration scenario, the soft and hard X-ray weakness of these quasars can be uniformly explained

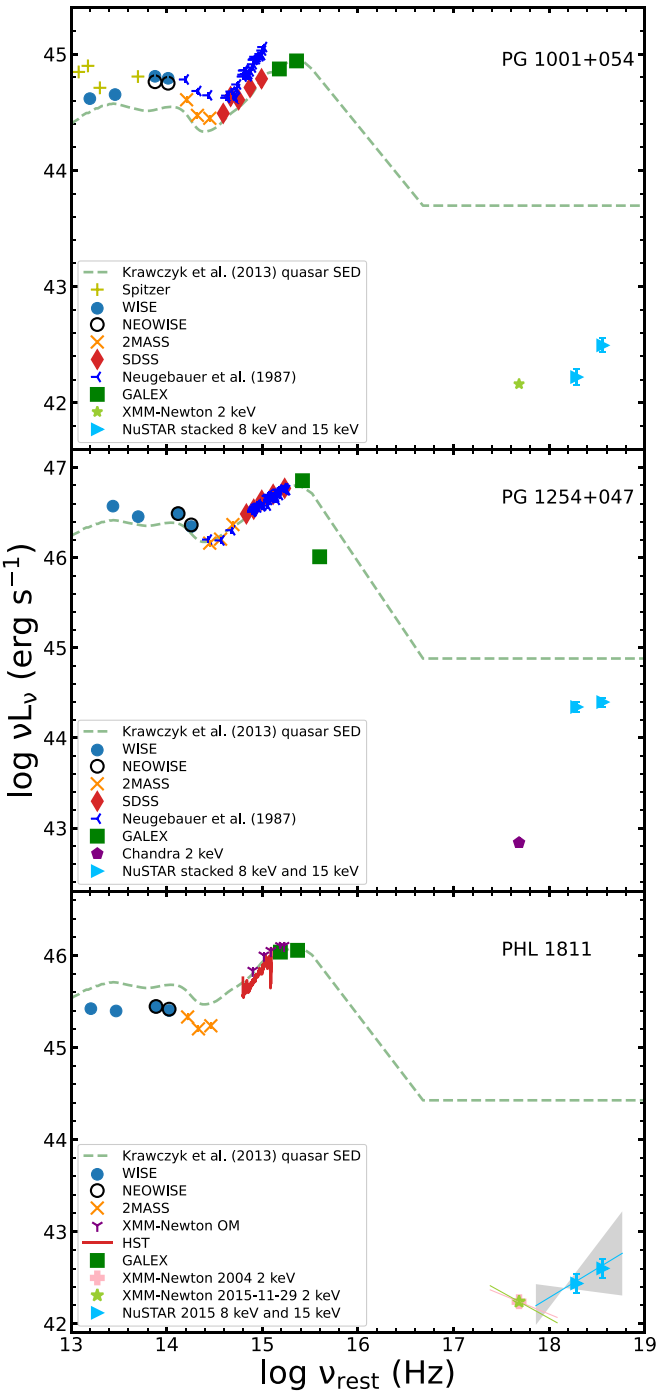

Figure 3. SEDs of the three quasars (see Section 3.3 for the IR–UV data). The 2 keV luminosities were derived from the power-law spectral fitting of the Chandra or XMM-Newton spectra (Section 3.1). The 8 and 15 keV luminosities were derived from the NuSTAR photometric results (Section 3.2). For PHL 1811, we show the soft X-ray spectral slopes (with negligible uncertainties) from the two XMM-Newton observations and the hard X-ray spectral slope (with the shaded area representing the uncertainties) constrained from the NuSTAR observation, which differ beyond the 1σ level. The green dashed curve in each panel shows the mean quasar SED from Krawczyk et al. (2013) normalized to the 2500 Å luminosity; the X-ray component is a $\Gamma = 2$ power-law continuum that follows the $\alpha_{\rm OX}$–$L_{2500\ \text{Å}}$ relation.

under an X-ray obscuration-only scenario, without invoking the extra mechanism of intrinsic X-ray weakness. The X-ray absorber in this case might be a clumpy accretion disk wind that provides variable partial covering absorption to the nuclear X-ray emission.

4.1. Presence of X-Ray Obscuration in PHL 1811

PHL 1811 was considered an intrinsically X-ray weak quasar without any absorption based mainly on the following properties: (1) significantly weak emission with a steep spectral shape ($\Gamma = 2.3 \pm 0.1$) in the 2004 XMM-Newton 0.3–5 keV spectrum, and (2) flux variability by a factor of ≈ 4 in 12 days (Leighly et al. 2007a). Hard X-ray (>5 keV) data were not available previously. The 2004 XMM-Newton spectrum of PHL 1811 is dominated by background above 5 keV, with a P_B value (see Section 3.2) of only 0.1 in the 5–10 keV band. In the deeper 2015 XMM-Newton observation, PHL 1811 was significantly detected in the 5–10 keV band, with a P_B value of 1.0×10^{-4} (3.9σ), allowing investigation of its hard X-ray properties. We first derived its photometric properties following the same procedure described in Section 3.2, though applied to the 0.3–10 keV band instead of the 3–24 keV band as for the NuSTAR data. The net source counts (without aperture correction) in the 0.3–2 keV and 2–10 keV bands are 872^{+35}_{-34} and 174^{+21}_{-20}, respectively, and the resulting 0.3–10 keV effective photon index ($\Gamma_{\rm eff,0.3-10}$) is 2.0 ± 0.1 from the band ratio of the above two bands and the spectral response files. If adopting a different set of energy bands, the 0.3–5 keV and 5–10 keV bands, the derived counts are 1000^{+39}_{-38} and 47^{+14}_{-13}, and the $\Gamma_{\rm eff,0.3-10}$ value becomes $1.8^{+0.1}_{-0.2}$. The slightly different $\Gamma_{\rm eff,0.3-10}$ values suggest that the spectral shape deviates from a simple power law.

We then fit the 2015 XMM-Newton 0.3–10 keV spectrum with a simple power-law model using XSPEC, under the assumption that PHL 1811 is an unabsorbed, intrinsically X-ray weak source. The spectrum was grouped with at least one count per bin, and the W statistic (see footnote 3) was used. The resulting photon index is $\Gamma = 2.57 \pm 0.09$; if limiting the energy range to 0.3–5 keV, the resulting Γ (2.63 ± 0.09) is consistent within the errors. The data and the best-fit model are shown in Figure 4(a), and there are significant residuals above $\approx$3 keV. It is possible that a Compton-reflection component from a distant reprocessor (e.g., the torus) contributes to the hard X-ray excess emission. We thus added an XSPEC `pexrav` component to the model with its photon index and normalization tied to those of the power-law component; the only free parameter is the reflection factor (reflection fraction), and the other parameters are fixed at their default values. The best-fit results are shown in Figure 4(b). The hard X-ray excess can be explained by the Compton-reflection component, but an unrealistically large reflection factor ($\approx$23) is required; the reflection factors for AGN samples are typically $\lesssim$2 (e.g., de Rosa et al. 2008; Ricci et al. 2011, 2017; Panagiotou & Walter 2019). We fixed the power-law photon index to 2.57 in the above test; when it was allowed to vary, a larger Γ ($\approx$3.0) and an even larger reflection factor ($\approx$81) were derived. Therefore, the 2015 XMM-Newton spectrum of PHL 1811 cannot be well described by a simple unabsorbed power-law continuum plus a reasonable amount of Compton reflection.

In Figure 4(a), the hard X-ray residuals peak around observed-frame 6 keV (rest-frame $\approx$7 keV), and we thus also considered a model where the hard X-ray excess has some contribution from a broad Fe Kα line produced via relativistic disk reflection (e.g., Ross & Fabian 2005; Fabian et al. 2013). We fit the 2015 XMM-Newton 0.3–10 keV spectrum with the XSPEC `relxill` model (Dauser et al. 2014; García et al. 2014). The free parameters are Γ, SMBH spin, ionization parameter, inclination angle, and reflection factor (reflection

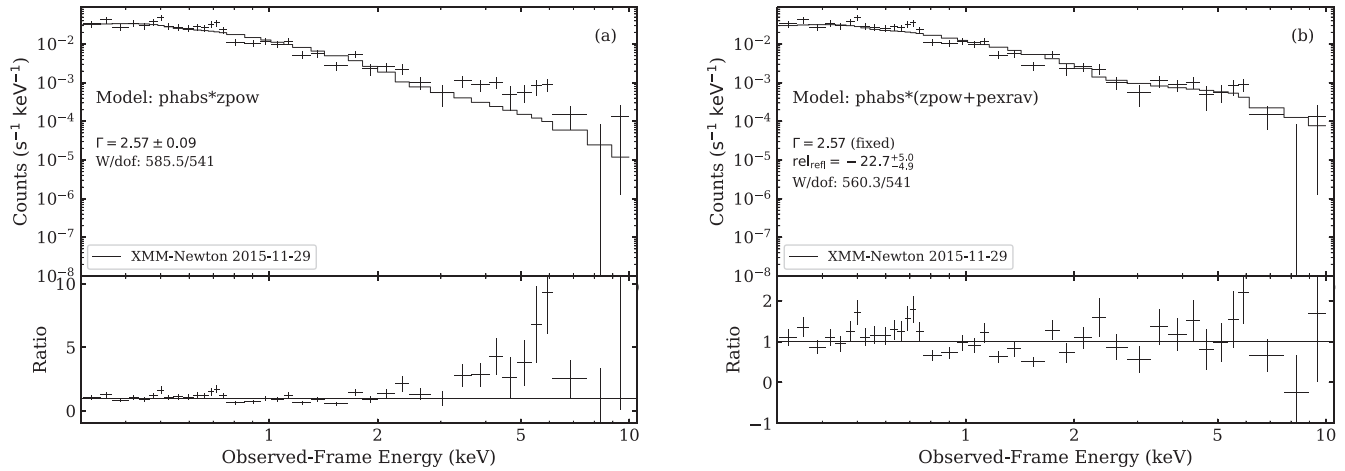

Figure 4. The 2015 XMM-Newton spectrum for PHL 1811 overlaid with the best-fit (a) simple power-law model and (b) simple power-law plus Compton-reflection model (with a fixed photon index). The spectra are grouped for display purposes only. The bottom panels display the ratios of the data to the best-fit models. Compared to the simple power-law model, there are significant fitting residuals above ≈3 keV, which require an unrealistically large reflection factor (≈23) to explain. The spectrum thus cannot be well described by a simple unabsorbed power-law continuum plus a reasonable amount of Compton reflection.

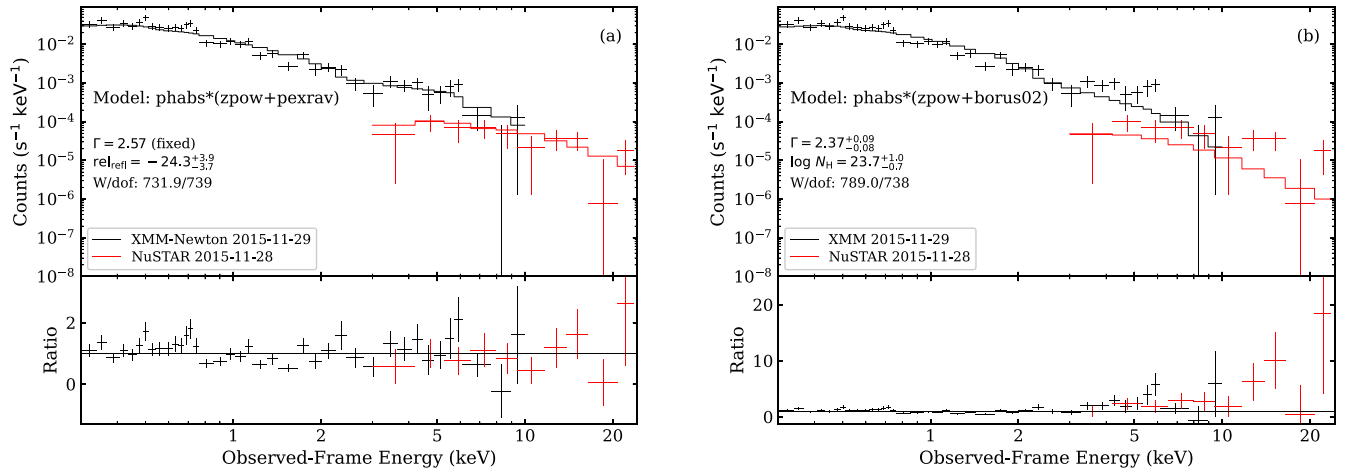

Figure 5. Similar to Figure 4, displaying the 2015 XMM-Newton and NuSTAR spectra for PHL 1811 overlaid with the best-fit power-law plus Compton-reflection model. The Compton-reflection component was modeled with (a) `pexrav` and (b) `borus02`. An unrealistically large reflection factor (≈24) is required in the `pexrav` model, while the self-consistent `borus02` Compton reflection is not sufficient to account for the excess emission in the hard X-rays.

fraction), and the other parameters were fixed at their default values. This model describes well the spectrum with similar residuals to those in Figure 4(b), with a best-fit Γ value of 2.02 ± 0.06 and a best-fit reflection factor of 10^{+65}_{-1}. The Γ value is smaller than 2.57 because the soft X-rays are now dominated by ionized disk reflection instead of an intrinsic power-law continuum. The reflection factor is still large, but unlike the Figure 4(b) modeling with a distant reflector, relativistic reflection from the inner accretion disk could produce an extremely large reflection factor if much of the coronal emission cannot reach the observer owing to the light-bending effects near the SMBH (e.g., Dauser et al. 2014). Nevertheless, a reflection-dominated spectrum with strong light-bending effects is still in contrast with the scenario of intrinsic X-ray weakness, where the observed spectrum should be dominated by the intrinsic power-law continuum from a weak corona.

The 3–24 keV spectral shape constrained from the 2015 simultaneous NuSTAR observation, $\Gamma_{\rm eff} = 1.4^{+0.8}_{-0.7}$ (Section 3.2), provides additional support that the spectral shape likely deviates from a steep unabsorbed power law. We thus applied the above `zpow + pexrav` model to jointly fit the 2015 XMM-Newton + NuSTAR spectra and investigate whether the spectra can be explained by an unabsorbed, intrinsically weak power-law continuum plus typical Compton reflection. The results are shown in Figure 5(a), and they are consistent with those for the XMM-Newton spectrum alone (Figure 4(b)), requiring a huge reflection factor. We then tested replacing the `pexrav` component with the self-consistent Compton-reflection model `borus02` (Baloković et al. 2018) with the photon index and normalization tied to those of the power-law component. The complete XSPEC model is `phabs * (zpow + atable{borus02.fits})`, and the free parameters are the power-law normalization, photon index (Γ), and column density ($N_{\rm H}$) of the reprocessed component.[20] The best-fit results are displayed in Figure 5(b). There are still significant fitting residuals above ≈5 keV, demonstrating again that a typical level of Compton reflection cannot account for the excess emission in the hard X-rays.

[20] The other parameters of the `borus02` model are fixed at the default values, including a high-energy cutoff of 300 keV, an inclination angle of 60°, a torus covering factor of 0.5 (corresponding to a half-opening angle of 60°), and an iron relative abundance of 1.

The 2015 XMM-Newton and NuSTAR observations of PHL 1811 thus reveal that, in addition to a steep power-law ($\Gamma = 2.63 \pm 0.09$) continuum in the 0.3–5 keV band, there is significant hard X-ray ($\gtrsim$5 keV) excess emission. The excess emission can be modeled with Compton reflection of a soft X-ray continuum that is much stronger (by a factor of $\gtrsim$20) than the observed one. We note that, from the best-fit `zpow + pexrav` results in Figure 5(a), PHL 1811 was intrinsically X-ray weak by a factor of $\approx$ 140 compared to the Steffen et al. (2006) $\alpha_{\rm OX}$–$L_{2500\,\text{Å}}$ relation. If we instead assume that PHL 1811 was intrinsically X-ray normal (i.e., raising the power-law normalization by a factor of 140) and add a scaling factor to the power-law component `c * zpow + pexrav`, the spectra can be equally well described with $c = 0.7\%$ (1/140) and a reasonable reflection factor of 0.17 (24/140). A physical interpretation of the above model is that PHL 1811 was affected by Compton-thick absorption and the observed XMM-Newton and NuSTAR spectra were dominated by a fraction of the intrinsic continuum scattered by a large-scale highly ionized "mirror" ($f_{\rm scatter}$; typically within a few percent; e.g., Turner et al. 1997; Cappi et al. 2006; Ueda et al. 2007; Winter et al. 2009; Yamada et al. 2020; Gupta et al. 2021) in the soft X-rays and a reprocessed component from the absorber in the hard X-rays. The steep soft continuum could also represent a fraction ($f_{\rm leak}$) of the intrinsic continuum leaking through a clumpy absorber. Therefore, instead of employing intrinsic X-ray weakness plus an unrealistically large reflection factor, we could interpret the 2015 XMM-Newton and NuSTAR data of PHL 1811 with Compton-thick obscuration.

In addition, the second property mentioned above, the short-term soft X-ray variability between the two Chandra observations in 2001 (see, e.g., Figure 1), was used to argue against a large-scale scattered component ($f_{\rm scatter}$ above) dominating the 0.3–5 keV X-ray spectrum. However, from recent investigations of extreme X-ray weakness and extreme X-ray variability among super-Eddington accreting AGNs (e.g., SDSS J075101.42+291419.1 and samples from Liu et al. 2019, 2021; SDSS J081456.10+532533.5 from J. Huang et al., in preparation), it appears plausible that such weak, steep, and variable soft X-ray emission might originate from variable fractions ($f_{\rm leak}$) of leaked intrinsic continuum through a large solid-angle, high column density, clumpy (partial covering) absorber. Thus, fast variability and steep spectral shapes in the soft X-rays do not necessarily rule out X-ray obscuration. In summary, unlike the model considered previously where PHL 1811 lacks absorption, hard X-ray data suggest that X-ray obscuration may well be present.

4.2. An Obscuration-only Scenario without Intrinsic X-Ray Weakness

The 2013 NuSTAR observations of PG 1001 and PG 1254, with no hard-band detections or $\Gamma_{\rm eff}$ measurements, were not sufficiently constraining to establish that intrinsic X-ray weakness must be present, which motivated the present study with deeper NuSTAR observations. The deeper NuSTAR observations now provide hard-band detections and $\Gamma_{\rm eff}$ measurements (albeit with large uncertainties). The PG 1001 spectral shape appeared flatter in the 2020 observation ($\Gamma_{\rm eff} = 0.4^{+0.6}_{-0.9}$ compared to $\Gamma_{\rm eff} > 1.5$), suggesting the presence of absorption and probably spectral shape evolution between these two epochs. The stacked $\Gamma_{\rm eff}$ value ($1.0^{+0.5}_{-0.6}$) from the two NuSTAR observations is still small compared to the typical value of ≈ 2 for an unabsorbed spectrum. The PG 1254 spectral slope appears typical for unobscured quasars ($\Gamma_{\rm eff} = 1.8^{+0.5}_{-0.4}$ in the 2019 observation), but it is also clear that this quasar is X-ray weak by only a factor of a few in the hard X-rays (see Figure 3). Considering its significant soft X-ray weakness and the flat spectral shape in the soft X-rays (Section 3.1), the nominal hard X-ray spectral shape in the NuSTAR data might be explained by Compton-thin absorption. Since PG 1254 is at $z = 1.026$, we are likely observing the penetrating hard X-rays with NuSTAR through an absorber with a large but Compton-thin $N_{\rm H}$ value; this would explain the strong X-ray weakness at 2 keV and much reduced X-ray weakness at higher energies. As discussed in Section 4.1 above, hard X-ray data suggest that X-ray obscuration is also present in PHL 1811.

Motivated by these NuSTAR results, we argue that intrinsic X-ray weakness is probably not required to explain the extreme X-ray weakness of these quasars. We explore the possibility of interpreting universally the NuSTAR, Chandra, and XMM-Newton spectra with an obscuration-only scenario where these quasars are intrinsically X-ray normal (following the $\alpha_{\rm OX}$–$L_{2500\,\text{Å}}$ relation). We investigate below, via XSPEC spectral fitting, whether the multiepoch soft and hard X-ray spectra can be described by nominal-strength X-ray emission modified by our adopted obscuration model with the absorber parameters (the column density and partial covering fraction) allowed to vary. Since the X-ray data do not have sufficient statistics for complex spectral fitting, we had to simplify the model and fix many of the model parameters. Moreover, we actually cannot rule out the scenario of obscuration + intrinsic X-ray weakness, which has an extra degree of freedom (i.e., normalization of the X-ray continuum) compared to the obscuration-only scenario. Our focus here is to investigate whether we can explain the observed X-ray emission without involving intrinsic X-ray weakness from, e.g., an anomalous corona.

Although the `pexrav` model appears able to describe the PHL 1811 spectra well (Section 4.1 and Figure 5(a)), it does not provide constraints on the absorption column densities. We thus employed the self-consistent `borus02` model to describe the reprocessed component from the absorber. The XSPEC spectral model is

```
phabs * (zphabs * cabs * c1 * zpow
+c2 * zpow + atable{borus02.fits} ).
```

In this model, `phabs` accounts for the Galactic absorption, and `zpow` is the intrinsic power-law continuum that is X-ray normal with respect to the Steffen et al. (2006) $\alpha_{\rm OX}$–$L_{2500\,\text{Å}}$ relation. A large fraction (c_1) of the intrinsic continuum is modified by heavy neutral absorption (`zphabs`) and Compton scattering (`cabs`). The absorber is clumpy, allowing a fraction ($f_{\rm leak} = c_2 = 1 - c_1$) of the intrinsic continuum to leak through. There is probably also a large-scale scattered component ($f_{\rm scatter}$). Since the leaked component usually dominates, we treated them together and do not separate $f_{\rm scatter}$ from $f_{\rm leak}$ in the following study. The reprocessed component from the absorber is modeled with `borus02` with the normalization and photon index tied to those of `zpow`. We fixed the inclination angle to 60° and allowed the absorber covering factor to vary. The other `borus02` parameters were fixed at the default values (see footnote 9). We also tied the absorption column densities ($N_{\rm H}$) in the `zphabs`, `cabs`, and `borus02` components. The

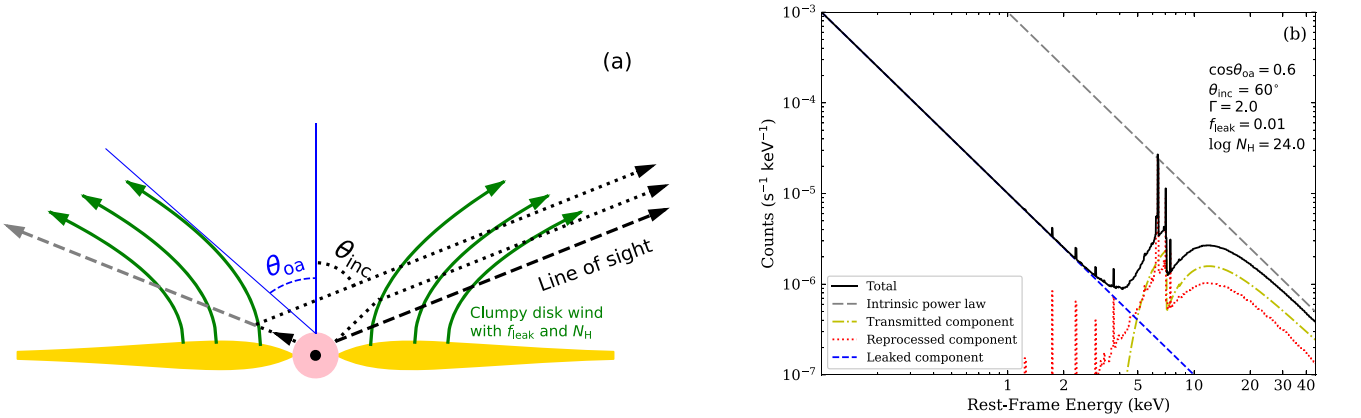

Figure 6. (a) A schematic diagram of the obscuration scenario. The black circle represents the SMBH, surrounded by the X-ray corona shown in pink. The yellow region represents the accretion disk. The green arrows represent the absorber (e.g., an outflowing disk wind) with a half-opening angle of θ_{oa} and a covering factor of $\cos\theta_{oa}$. The system inclination angle is θ_{inc}. The dashed line traces the transmitted (absorbed) radiation through the absorber in the direction of the observer (transmitted component). The dotted curves trace the radiation reflected from the opposite side of the absorber and the radiation scattered to the line of sight through the absorber (reprocessed component). The absorber is clumpy, allowing a fraction (f_{leak}) of the intrinsic continuum to leak through without being absorbed (leaked component). There is probably also a fraction ($f_{scatter}$) of the intrinsic continuum scattered to the line of sight by a large-scale highly ionized "mirror" (not shown in the cartoon). We treated f_{leak} and $f_{scatter}$ together in this model. (b) An example of the X-ray spectral components for a given set of the absorber parameters. The black solid curve shows the total observed model spectrum, while the gray long-dashed line, yellow dashed–dotted curve, red dotted curve, and blue dashed line represent the intrinsic power law, transmitted component, reprocessed component, and leaked component, respectively.

emergent spectrum is thus a combination of the transmitted (absorbed) component, leaked component, and reprocessed component. A schematic illustration of the setup is shown in Figure 6(a), and an example of the X-ray spectral components for a given set of the absorber parameters is displayed in Figure 6(b).

There are a couple of caveats regarding the above model. First, the absorber is probably partially ionized instead of being neutral. Ionized absorption produces distinctive spectral features below ≈1 keV, but the continuum shapes above ≈1 keV are similar to those from neutral absorption unless the ionization level is high (e.g., Figure 1 of Netzer 1993). For the three quasars studied here, PG 1254 has few photons below 1 keV, PHL 1811 shows no absorption signatures below ≈5 keV, and PG 1001 has clear soft X-ray excess emission in the 0.3–1 keV band, which was interpreted with ionized absorption (Schartel et al. 2005). Their >1 keV spectra do not have sufficient photon statistics to distinguish ionized absorption from neutral absorption or constrain reliably ionization parameters. Therefore, in the above model, we adopted neutral absorption for simplicity, and we did not use the <1 keV XMM-Newton or Chandra data for PG 1001. The soft excess of PG 1001 in the obscuration scenario will be discussed in Section 4.2.1. Second, since there is no optical/UV extinction, the absorber should not be the torus described in the `borus02` model with a toroidal geometry. Instead, it is likely a small-scale clumpy dust-free wind launched from the accretion disk (see Section 4.3). Therefore, the `borus02` model does not provide an accurate description of the reprocessed emission (both the continuum and the Fe Kα line) from the absorber (e.g., wind). However, since our purpose here is not to recover precise absorber parameters but to simply investigate whether the obscuration-only scenario is a valid alternative to the scenario of intrinsic X-ray weakness + obscuration, and the current simplified model appears able to explain reasonably well the multiepoch X-ray spectra of the three quasars (as discussed below), we defer detailed modeling to future studies, which likely will require much better spectral quality.

We applied the above model to explain the multiepoch X-ray spectra of the three quasars. We jointly fit the NuSTAR, Chandra, and XMM-Newton spectra for each of the three quasars. The free parameters are Γ, f_{leak} (c_2), N_H, and the absorber covering factor ($\cos\theta_{oa}$ in Figure 6(a)); f_{leak} and N_H were allowed to vary between the observations, while the other two parameters were tied. In addition, for the latest NuSTAR observation of PG 1001 and the two NuSTAR observations of PG 1254, we tied the f_{leak} parameter to that of the nonsimultaneous Chandra observation, as the NuSTAR spectra are not sensitive to this parameter (high-energy spectra do not have a significant leaked component). These quasars are considered to be intrinsically X-ray normal, with the intrinsic $f_{2\ keV}$ values fixed at those expected from the Steffen et al. (2006) α_{OX}–$L_{2500\ Å}$ relation. The $f_{2\ keV}$ and Γ values define the intrinsic continua (normalizations of `zpow`). For each object, the `zpow` normalization was first fixed at the value derived with $\Gamma = 2$, and then an iterative procedure was performed to adjust the `zpow` normalization according to the best-fit Γ value. A few iterations were needed until the intrinsic continuum converged.

The best-fit parameters are listed in Table 3, and the best-fit models are displayed in Figure 7. We also list in Table 3 the main components (transmitted, reprocessed, and/or leaked) that dominate the emergent spectrum of each observation. The Γ values for PG 1001 and PHL 1811 pegged at 2.6, the upper bound allowed by the `borus02` model. Several N_H values do not have upper errors, as the emergent spectrum is dominated by the leaked component, which is not sensitive to N_H; a few of these pegged at $\log N_H/\mathrm{cm}^{-2} = 25.5$, the upper bound allowed by the `borus02` model. The fitting results are acceptable overall considering the fitting statistics (W/dof; Figure 7) and residuals, indicating that the obscuration scenario is able to explain the multiepoch X-ray data without involving intrinsic X-ray weakness. From the best-fit models, we computed the f_w values for the NuSTAR spectra, and these are also listed in Table 3. These hard X-ray weakness factors are comparable to

Table 3
Best-fit Parameters for the Multiepoch X-Ray Spectral Fitting

Object Name	Observatory	Obs. Date	$\cos\theta_{oa}$	Partial Covering Absorption			f_w[a]	Main Com.[b]
				f_{leak}	Γ	$\log N_H$ (cm^{-2})		
PG 1001	XMM-Newton	2003 May 4	$0.54^{+0.06}_{-0.07}$	$1.9^{+0.4}_{-0.3}\times10^{-2}$	$2.6_{-0.02}$ [d]	23.5 ± 0.1	⋯	leak, tra
PG 1001	Chandra	2010 Jan 11	⋯	$7.5^{+4.6}_{-3.5}\times10^{-3}$	⋯	$23.7^{+1.3}_{-0.2}$	⋯	leak, tra
PG 1001	NuSTAR	2013 Jun 28	⋯	0.10 ± 0.05	⋯	$24.3^{+0.9}_{-0.2}$	16.7	leak, rep
PG 1001	NuSTAR	2020 May 23	⋯	7.5×10^{-3} (tied)	⋯	24.2 ± 0.1	52.7	tra, rep
PG 1254	Chandra	2000 May 29	$0.38^{+0.06}_{-0.19}$	$7.4^{+2.7}_{-2.1}\times10^{-3}$	$2.12^{+0.03}_{-0.09}$	$25.5_{-1.0}$	⋯	leak, rep
PG 1254	NuSTAR	2013 Jun 8	⋯	–(tied)	⋯	24.0 ± 0.2	8.7	tra, rep
PG 1254	NuSTAR	2019 Jun 8	⋯	–(tied)	⋯	$23.6^{+0.2}_{-0.1}$	3.2	tra
PHL 1811	Chandra	2001 Dec 5	$0.58^{+0.01}_{-0.02}$	$6.0^{+0.8}_{-0.7}\times10^{-3}$	$2.6_{-0.05}$	$24.1^{+0.5}_{-0.2}$	⋯	leak, rep
PHL 1811	Chandra	2001 Dec 17	⋯	$(2.8\pm0.2)\times10^{-2}$	⋯	$24.9_{-0.5}$	⋯	leak
PHL 1811	XMM-Newton	2004 Nov 1	⋯	$(6.7\pm0.4)\times10^{-3}$	⋯	$25.5_{-0.5}$	⋯	leak
PHL 1811	XMM-Newton	2015 Nov 29	⋯	$(7.4\pm0.3)\times10^{-3}$	⋯	$24.6_{-0.2}$	⋯	leak, rep
PHL 1811	NuSTAR	2015 Nov 28	⋯	$(1.1\pm0.8)\times10^{-2}$	⋯	24.8 ± 0.2	98.3	leak, rep
PHL 1811	XMM-Newton + NuSTAR[c]	2015 Nov	⋯	$(7.4\pm0.3)\times10^{-3}$	⋯	$24.8^{+0.4}_{-0.2}$	⋯	leak, rep

Notes.
[a] The factor of X-ray weakness at rest-frame 8 keV derived from the best-fit model, for comparison with the results in Table 2.
[b] The "Main Com." column lists the dominant component/components in the emergent spectrum: "leak" represents the leaked/scattered component, "tra" represents the transmitted (absorbed) component through the absorber (dashed line in Figure 6), and "rep" represents the reprocessed component from the absorber (dotted curves in Figure 6).
[c] In this case, the fitting parameters for the XMM-Newton and NuSTAR observations were tied.
[d] A value without an upper error is effectively bound by the allowed upper bound of the `borus02` model.

those listed in Table 2, and any discrepancy is mainly due to the different models used (a simple power-law model is assumed in deriving the photometric results in Table 2).

Given the limited X-ray data quality and the simplifications/assumptions made during the modeling process, we do not consider these spectral fitting results fully accurate descriptions of the absorber properties. Nevertheless, they provide important clues for explaining the unusual X-ray properties under our proposed obscuration-only scenario. The best-fit results are consistent with our qualitative expectation above. The multiepoch spectra of PG 1001 are explained by heavy or even Compton-thick obscuration. A strong leaked component is required to explain its 2013 NuSTAR spectrum, as the spectral shape is likely steeper than an absorbed power law ($\Gamma_{eff} > 1.5$), while the 2020 NuSTAR spectrum is affected by typical Compton-thick obscuration. The Chandra spectrum of PG 1254 requires very Compton-thick obscuration due to the significant weakness of this $z \approx 1$ spectrum. The NuSTAR observations of PG 1254 are explained by heavy but Compton-thin obscuration. PHL 1811 was almost always affected by Compton-thick obscuration, and the emergent spectra are largely dominated by the leaked component (though with small f_{leak} values). The reprocessed component does not contribute much, as the absorber appears to have a large covering factor ($\cos\theta_{oa} \approx 0.6$), which blocks direct reflected radiation from the opposite side of the absorber (see, e.g., the top dotted curve in Figure 6). Therefore, PHL 1811 can reach a very large hard X-ray weakness factor (f_w) in the NuSTAR observation. For the 2015 simultaneous XMM-Newton and NuSTAR observations of PHL 1811, the derived parameters differ slightly. We also tried to tie all the parameters in these two observations, and the results are listed in the last row of Table 3. We do not consider the small discrepancy a serious issue, as there may be cross-calibration uncertainties between the XMM-Newton and NuSTAR data (e.g., Madsen et al. 2021).

4.2.1. Soft X-Ray Excess of PG 1001 in the Obscuration-only Scenario

Soft X-ray excess emission (typically below ≈1 keV) is observed in a large fraction of type 1 AGNs, the origin of which is still under debate and may be attributed to ionized absorption (e.g., George et al. 1998; Gierliński & Done 2004), ionized disk reflection (e.g., Ross & Fabian 2005; Crummy et al. 2006), or Comptonization in a warm corona (e.g., Done et al. 2012). Of the three quasars in this study, only PG 1001 shows a clear soft-excess component in both its XMM-Newton and Chandra spectra. We thus did not consider the soft excess in the above modeling, excluding the <1 keV data for PG 1001. We explore here whether the soft X-ray excess emission of PG 1001 can be explained in the obscuration-only scenario. We focus on the XMM-Newton spectrum in the following discussion, as the Chandra spectrum has only 19 counts in the 0.3–8 keV band. Nevertheless, we verified that the Chandra spectrum yields consistent results.

The soft-excess emission of PG 1001 is at a comparable flux level to the >1 keV power-law component that is significantly weak compared to the expectation from the α_{OX}–$L_{2500\,Å}$ relation (Section 3.1.1). Therefore, the soft excess is also significantly weak compared to typical levels. In the obscuration-only scenario, PG 1001 has a nominal-strength hot corona and likely also a nominal-strength warm corona. A natural interpretation would then be that the soft-excess emission is also filtered by the absorber if it is from the warm corona. We thus fitted the 0.3–10 keV XMM-Newton spectrum with the same model described in Section 4.2 plus an additional component to describe the soft excess from the warm corona. We tested simple power-law (`zpow`), disk multiblackbody (`diskbb`), or Comptonization (`compTT`) models for this soft-excess component, and the three choices were all able to describe the spectrum well with comparable statistics. In Figure 8, we show the best-fit results with the power-law model. The soft excess has a large photon index (≈5.0) and a small normalization (≈0.7% of the normalization for the

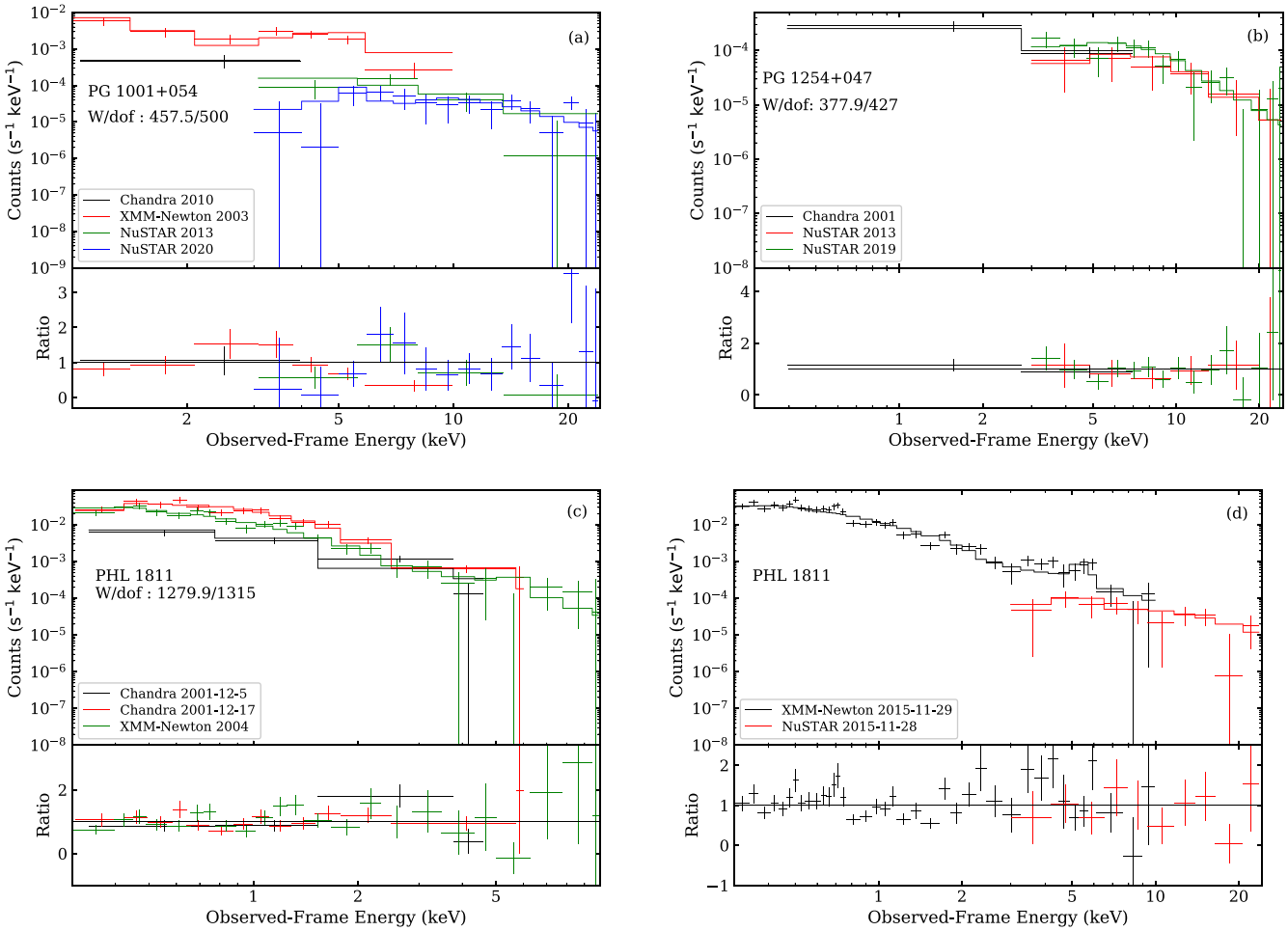

Figure 7. The Chandra, XMM-Newton, and NuSTAR spectra for the three quasars, overlaid with the best-fit models using the obscuration model described in Section 4.2. The spectra are grouped for display purposes only. The bottom panels display the ratios of the data to the best-fit models. We break the five observations of PHL 1811 into two panels for clarity. For PG 1001, the energy ranges used are 1–8 keV for the Chandra observation and 1–10 keV for the XMM-Newton observation owing to the apparent soft X-ray excess emission at lower energies. The obscuration scenario explains reasonably well the multiepoch broadband X-ray spectra of the three quasars.

intrinsic >1 keV power-law continuum), and the other free parameters ($f_{\rm leak}$ and $N_{\rm H}$) are consistent with those in Table 3 (first row) within the errors. One interpretation is thus that the observed soft excess is the leaked portion of the warm corona emission through the same dust-free absorber, and the leaked fraction is similar to or even the same as that for the main component.

The soft X-ray excess emission of PG 1001 has also been suggested to be due to ionized absorption (Schartel et al. 2005). We verified that the 0.3–10 keV XMM-Newton spectrum can be acceptably fitted with a simple partial covering ionized absorption model (`zxipcf * zpow`), fixing $\Gamma = 2.6$ and the power-law normalization at the X-ray nominal value from the $\alpha_{\rm OX}$–$L_{2500\,\text{Å}}$ relation. The resulting ionization parameter is $\xi \approx 91$ erg cm s^{-1} with $N_{\rm H} \approx 4.7 \times 10^{23}$ cm^{-2} and a covering fraction of ≈99.1%. Replacing the neutral absorption (`zphabs`) in the Section 4.2 model with `zxipcf` yields consistent results, as the reprocessed component (`borus02`) is not important in the XMM-Newton spectrum. The soft excess can thus also be explained with ionized absorption, which is possible considering that the absorber (e.g., disk wind) is probably partially ionized. Overall, we consider that our proposed obscuration-only scenario can plausibly explain the soft X-ray excess emission of PG 1001.

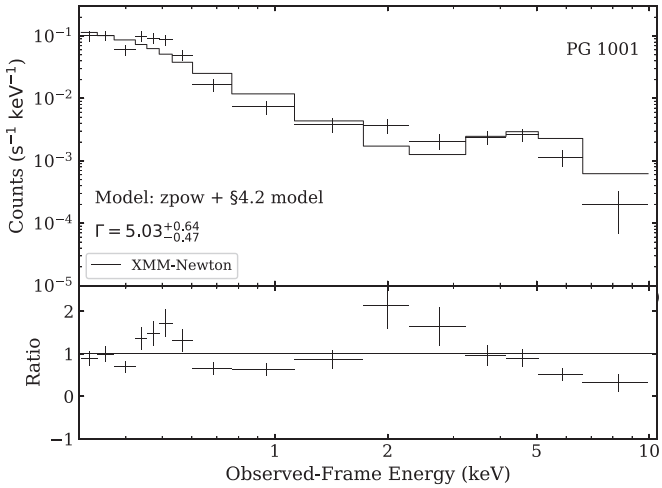

Figure 8. The 0.3–10 keV XMM-Newton spectrum of PG 1001 fitted with the Section 4.2 model plus an additional power-law component. The spectrum is grouped for display purposes only. The bottom panel displays the ratios of the data to the best-fit model. The additional power-law component describes well the soft-excess emission with a large photon index of ≈5.0. The soft excess is probably the leaked portion of the warm corona emission through the same dust-free absorber that obscures the >1 keV main component.

4.3. Clumpy Accretion Disk Wind as the Absorber and Implications

Under our proposed obscuration scenario above, PG 1001 and PG 1254 are BAL quasars with intrinsically normal X-ray emission. Thus, they are probably similar to the typical BAL quasars that generally show X-ray obscuration. Besides the few low-redshift BAL quasars with NuSTAR observations (Luo et al. 2013, 2014; Teng et al. 2014), a few high-redshift BAL quasars have been suggested to be intrinsically X-ray weak (Liu et al. 2018). From the systematic Chandra survey of the 29 high-ionization LBQS BAL quasars at $z \approx 2$, two intrinsically X-ray weak candidates were identified based on their nominal spectral shapes ($\Gamma_{\rm eff} \approx 2$) and significant hard X-ray weakness factors ($f_w \approx 12$–15); at these redshifts, Chandra observations were able to provide rest-frame hard X-ray constraints over a similar band to the NuSTAR observations of low-redshift objects. We recently obtained a long XMM-Newton observation for one of the candidates, LBQS 1442–0011. The observation was heavily affected by background flares, and the cleaned exposure time is only 40% of the total. The results are summarized in the Appendix. The XMM-Newton observation suggests that the spectral shape became flatter ($\Gamma_{\rm eff} \approx 1$) and the factor of hard X-ray weakness (f_w) also dropped to ≈4. We thus consider that the X-ray weakness of this quasar can also be described by our proposed scenario of variable obscuration, without invoking intrinsic X-ray weakness. It is natural to consider that the X-ray absorbers in PG 1001, PG 1254, and LBQS 1442–0011 are similar to those in typical BAL quasars, i.e., the shielding gas or clumpy accretion disk wind. They might have an extreme version of the absorber in terms of its high column density and/or large covering factor.

An obscuration explanation for the X-ray weakness of PHL 1811 would connect it with the PHL 1811 analogs studied in Luo et al. (2015). PHL 1811 and its analogs belong to a broader category of quasars, weak emission-line quasars (WLQs), a small population of type 1 quasars that show unusually weak UV emission lines (e.g., C IV). Systematic X-ray surveys of WLQ samples have revealed that a large fraction (≈30%–50%) of them are X-ray weak (e.g., Luo et al. 2015; Ni et al. 2018, 2022; Pu et al. 2020). These WLQs have typically been selected to lie at $z \gtrsim 1.5$, and thus Chandra or XMM-Newton observations provide rest-frame hard X-ray constraints. The individual and stacked effective power-law photon indices for the X-ray weak WLQs are in general flat ($\Gamma_{\rm eff} \approx 1.2$), suggesting an obscuration scenario. The absorber is proposed to be the geometrically thick inner accretion disk and/or its associated disk wind, which also shields the nuclear EUV/X-ray ionizing radiation from reaching the BELR, causing the weak emission lines. Thick inner accretion disks are expected in WLQs, as they are considered to have high or even super-Eddington accretion rates that result in thick disks (e.g., Abramowicz et al. 1988; Mineshige et al. 2000; Wang & Netzer 2003; Ohsuga & Mineshige 2011; Jiang et al. 2014). Powerful accretion disk winds launched via radiation pressure are expected in such systems (e.g., Takeuchi et al. 2014; Jiang et al. 2019; Giustini & Proga 2019). PHL 1811 likely has a super-Eddington accretion rate, and the large covering factor absorber is probably the strong wind associated with a thick accretion disk.

Therefore, the three quasars in this study likely share a similar nature, with partial covering absorption from clumpy dust-free winds (e.g., Figure 6). X-ray absorption from clumpy winds/outflows has been observed in typical type 1 AGNs (e.g., Kaastra et al. 2014; Mehdipour et al. 2017, 2021; Dehghanian et al. 2019; Laha et al. 2021), although the absorption strength is often not comparable to the extreme X-ray weakness found in our three quasars. The wind strength and density likely have an Eddington ratio dependence, as heavy or even Compton-thick absorption has been observed in super-Eddington accreting AGNs (e.g., Longinotti et al. 2019; Liu et al. 2021). The three quasars in this study probably have super-Eddington accretion rates that drive powerful and high-density clumpy winds. They have large estimated Eddington ratios as listed in Table 1. We note that these Eddington ratios do not represent accurately the accretion power in the super-Eddington regime, as a large fraction of the power may be advected into the SMBH or converted into mechanical energy of the wind (e.g., Jiang et al. 2019; see also Section 2.1 for further discussion). The large intrinsic X-ray photon indices derived from spectral fitting ($\Gamma \approx 2.1$–2.6; Table 3) also suggest super-Eddington accretion rates (e.g., Shemmer et al. 2008; Huang et al. 2020). The NLQ1 classification and the weak [O III] emission of PG 1001 and PHL 1811 (Section 2.1) provide additional support of super-Eddington accretion in these two quasars (e.g., Boroson & Green 1992; Sulentic et al. 2000; Shen & Ho 2014).

It is somewhat odd that PG 1001 shows a strong C IV emission line in its UV spectrum (Brandt et al. 2000), as the strong and high-density wind and/or the thick inner accretion disk should be able to shield the BELR from the nuclear ionization, resulting in a WLQ like PHL 1811. It also appears unusual that PHL 1811 does not show any significant UV absorption lines (i.e., BALs). Perhaps the dynamical nature of the wind (e.g., variable $N_{\rm H}$ and covering factor) causes the apparent discrepancy, and multiepoch UV spectra might be able to shed some light. For example, a $z \approx 2$ WLQ has recently been found to undergo BAL transformation (Yi et al. 2022). Geometric effects might also play a role, as the line of sight to the X-ray corona, the line of sight to the accretion disk UV continuum region, and the direction from the nucleus to the BELR are different from each other, and thus the emergent X-ray and UV spectra depend on the physical configuration of the clumpy wind (e.g., Giustini & Proga 2019).

Although our proposed obscuration scenario was based on the new sensitive NuSTAR observations of these three quasars, the general connection with obscuration from the disk wind suggests that this scenario may be applicable to the other intrinsically X-ray weak quasar candidates (e.g., those in Nardini et al. 2019; Laurenti et al. 2022). Obscuration from the clumpy disk wind would predict X-ray variability from varying obscuration. For the three quasars in this study, PG 1001 and PHL 1811 showed clear soft X-ray variability (e.g., Figure 1); the 12-day variability timescale of PHL 1811 does not provide any strong constraints on the wind velocity, as a wind clump only needs to move a fraction of the corona size. The NuSTAR observations of PG 1001 suggest some hard X-ray variability, at least in the spectral shape (Table 2). The PG 1254 NuSTAR observations do not provide sufficient photon statistics to identify hard X-ray variability. In addition, LBQS 1442–0011 likely has hard X-ray variability (see the Appendix). The WLQs have limited multiepoch observations, and a few of them have been found to vary strongly between X-ray normal and X-ray weak states (Miniutti et al. 2012; Ni et al. 2020). A small fraction of super-Eddington accreting AGNs have also

been found to vary between X-ray normal and X-ray weak states (e.g., Liu et al. 2019; Boller et al. 2021; Liu et al. 2021), and a few also show steep spectra in the low state. Another characteristic property of such X-ray variability is that there is no contemporaneous optical/UV continuum or emission-line variability, which argues against changes of accretion rates and supports the obscuration scenario. This property also makes these AGNs distinct from the unusual population of "changing-look" AGNs (e.g., 1ES 1927 + 654; Trakhtenbrot et al. 2019; Ricci et al. 2021) that also show extreme X-ray variability but are generally attributed to changes of accretion rates or tidal disruption events. Multiepoch X-ray observations of the intrinsically X-ray weak quasar candidates might be able to reveal X-ray variability and help clarify their nature.

5. Summary and Future Work

In this paper, we used NuSTAR observations of PG 1001, PG 1254, and PHL 1811 to constrain their hard X-ray ($\gtrsim$5 keV) weakness and spectral shapes and thus to investigate the nature of their extreme X-ray weakness. These quasars show very weak soft X-ray emission (Figure 1), and they were previously proposed to be intrinsically X-ray weak, with the X-ray coronae producing weak continuum emission relative to their optical/UV emission (deviating below the $\alpha_{\rm OX}$–$L_{2500\,\text{Å}}$ relation). The multiepoch soft and hard X-ray observations are summarized in Table 1. NuSTAR aperture photometry was presented in Section 3.2, and the results are summarized in Table 2 and Figure 3. The NuSTAR spectral shapes for PG 1001 and PHL 1811 appear flat ($\Gamma_{\rm eff} = 1.0^{+0.5}_{-0.6}$ and $\Gamma_{\rm eff} = 1.4^{+0.8}_{-0.7}$, respectively), while the shape is nominal for PG 1254 ($\Gamma_{\rm eff} = 1.8 \pm 0.3$). PG 1001 and PHL 1811 are significantly hard X-ray weak compared to the expectations from their optical/UV emission (f_w at 8 keV $\approx$ 26–74), while PG 1254 is only X-ray weak by a factor of $\approx$3. The PHL 1811 hard X-ray photon index appears smaller than its soft X-ray (0.3–5 keV) photon index (2.3 ± 0.1). Spectral modeling suggests that its 2015 XMM-Newton and NuSTAR spectra cannot be described by an intrinsically weak continuum plus a reasonable amount of Compton reflection (Section 4.1 and Figures 4 and 5).

In light of the new NuSTAR results, a variable X-ray absorber can account for all the observations of these X-ray weak quasars. We propose that, as an alternative to the intrinsic X-ray weakness + X-ray obscuration scenario, the soft and hard X-ray weakness of these quasars can be uniformly explained under an X-ray obscuration-only scenario, without invoking the extra mechanism of intrinsic X-ray weakness (Section 4.2). In this scenario, the weak emergent spectrum is a combination of the transmitted component modified by absorption, the leaked component through a clumpy absorber (including a distant scattered component), and the reprocessed component reflected/scattered from the absorber (Figure 6). This partial covering absorption scenario provides adequate explanations of the multiepoch X-ray data of these quasars, and the X-ray variability is mainly induced by the varying column density and leaked fraction (partial covering fraction) of the absorber (Table 3 and Figure 7).

We propose that the absorber is a clumpy dust-free wind launched from the accretion disk (Section 4.3). These quasars probably have super-Eddington accretion rates that result in geometrically thick inner accretion disks and powerful winds with high column densities and large covering factors. Although we cannot rigorously prove that intrinsic X-ray weakness is not present in these systems, the connections of these quasars to other X-ray weak quasars, including WLQs and super-Eddington accreting quasars, point to a universal wind obscuration scenario for the weak X-ray emission found in type 1 quasars, or even type 1 AGNs in general. Multiepoch X-ray observations of the intrinsically X-ray weak quasar candidates will further help clarify their nature. Besides variability investigations, deeper NuSTAR observations of PHL 1811 could provide further evidence of heavy X-ray obscuration. In addition, higher signal-to-noise ratio and higher spectral resolution observations with future-generation X-ray observatories (e.g., Athena; Nandra et al. 2013) could reveal spectral features (e.g., the Fe lines in the reprocessed component) that help discriminate between different scenarios.

C.W. and B.L. acknowledge financial support from the National Natural Science Foundation of China grant 11991053 and China Manned Space Project grant Nos. CMS-CSST-2021-A05 and CMS-CSST-2021-A06. W.N.B. acknowledges support from the V. M. Willaman Endowment, NASA grants 80NSSC20K0029 and 80NSSC22K0071, and Penn State ACIS Instrument Team contract SV4-74018 (issued by the Chandra X-ray Center, which is operated by the Smithsonian Astrophysical Observatory for and on behalf of NASA under contract NAS8-03060). F.E.B acknowledges support from ANID-Chile BASAL AFB-170002 and FB210003, FONDECYT Regular 1200495 and 1190818, and Millennium Science Initiative ProgramICN12_009. S.C.G thanks the Natural Science and Engineering Research Council of Canada.

We have made use of data from the NuSTAR mission, a project led by the California Institute of Technology, managed by the Jet Propulsion Laboratory, and funded by the National Aeronautics and Space Administration. We thank the NuSTAR Operations, Software, and Calibration teams for support with the execution and analysis of these observations. This research has made use of the NuSTAR Data Analysis Software (NuSTARDAS) jointly developed by the ASI Science Data Center (ASDC, Italy) and the California Institute of Technology (USA).

The Chandra ACIS Team Guaranteed Time Observations (GTO) utilized were selected by the ACIS Instrument Principal Investigator, Gordon P. Garmire, currently of the Huntingdon Institute for X-ray Astronomy, LLC, which is under contract to the Smithsonian Astrophysical Observatory via contract SV2-82024.

Appendix
XMM-Newton Observation of LBQS 1442–0011

LBQS 1442–0011 is a BAL quasar at $z = 2.226$ with a B-band magnitude of 18.2 (Gallagher et al. 2006). Its Hβ-based single-epoch virial SMBH mass is $\approx 8 \times 10^9\ M_\odot$, and its estimated Eddington ratio is $\approx$0.17 (Yuan & Wills 2003). Its previous Chandra observations have a co-added depth of 15.9 ks. Through systematic analyses of the Chandra observations of the Gallagher et al. (2006) LBQS BAL quasar sample, Liu et al. (2018) identified LBQS 1442–0011 as one of the two good candidates for intrinsically X-ray weak quasars based on its significant hard X-ray weakness (by a factor of $f_{\rm w} = 12^{+12}_{-8}$) and its nominal hard X-ray spectral shape ($\Gamma_{\rm eff} = 1.9^{+0.9}_{-0.8}$). The other candidate is LBQS 1203+1530.

Due to the large uncertainties of the f_w and $\Gamma_{\rm eff}$ values from the Chandra results, we proposed deeper XMM-Newton observations of the two candidates, aiming to improve the parameter constraints. The targets were accepted at priority C, and LBQS 1442–0011 was observed on 2021 February 6 with a nominal exposure time of 87 ks. Unfortunately, the observation was affected significantly by background flares, and the cleaned exposure time is only 34 ks. Thus, the sensitivity of the new XMM-Newton observation is only comparable to the previous co-added Chandra exposure. We processed the XMM-Newton data following the procedure described in Section 2.3. We chose a smaller source extraction region with a radius of 25″ in order to increase the signal-to-noise ratio of this faint source. We also limited the upper-energy bound to 8 keV. The resulting net source counts are 48^{+18}_{-17} in the 0.3–2 keV band (rest-frame 1.0–6.5 keV) and 33^{+15}_{-14} in the 2–8 keV band (rest-frame 6.5–26 keV). The $\Gamma_{\rm eff,0.3-8}$ value inferred from the band ratio is $1.0^{+0.7}_{-0.6}$. We also fit the spectrum with a power-law model modified by Galactic absorption (`phabs * zpow`), and the best-fit Γ value (0.9 ± 0.4) is consistent with the photometric result. The derived factor of hard X-ray weakness is $f_w = 4 \pm 2$.

Compared to the previous Chandra constraints, the XMM-Newton results suggest that the hard X-ray spectrum became flatter and the observed hard X-ray emission became brighter (f_w dropped). Therefore, we suggest that the X-ray weakness of LBQS 1442–0011 is also caused by variable partial covering absorption, similar to the three quasars studied here (see Section 4.3 for discussion).

ORCID iDs

B. Luo https://orcid.org/0000-0002-9036-0063
W. N. Brandt https://orcid.org/0000-0002-0167-2453
D. M. Alexander https://orcid.org/0000-0002-5896-6313
F. E. Bauer https://orcid.org/0000-0002-8686-8737
S. C. Gallagher https://orcid.org/0000-0001-6217-8101
Jian Huang https://orcid.org/0000-0002-9335-9455
Hezhen Liu https://orcid.org/0000-0003-0582-9558
D. Stern https://orcid.org/0000-0003-2686-9241

References

Abramowicz, M. A., Czerny, B., Lasota, J. P., & Szuszkiewicz, E. 1988, ApJ, 332, 646
Arnaud, K. A. 1996, in ASP Conf. Ser. 101, Astronomical Data Analysis Software and Systems V, ed. G. H. Jacoby & J. Barnes (San Francisco, CA: ASP), 17
Baloković, M., Brightman, M., Harrison, F. A., et al. 2018, ApJ, 854, 42
Baskin, A., Laor, A., & Stern, J. 2014, MNRAS, 445, 3025
Bellm, E. C., Kulkarni, S. R., et al. 2019, PASP, 131, 018002
Boller, T., Liu, T., Weber, P., et al. 2021, A&A, 647, A6
Boroson, T. A., & Green, R. F. 1992, ApJS, 80, 109
Brandt, W. N., Laor, A., & Wills, B. J. 2000, ApJ, 528, 637
Cappi, M., Panessa, F., Bassani, L., et al. 2006, A&A, 446, 459
Cardelli, J. A., Clayton, G. C., & Mathis, J. S. 1989, ApJ, 345, 245
Chen, C.-T. J., Hickox, R. C., Goulding, A. D., et al. 2017, ApJ, 837, 145
Comastri, A., Ranalli, P., Iwasawa, K., et al. 2011, A&A, 526, L9
Crummy, J., Fabian, A. C., Gallo, L., & Ross, R. R. 2006, MNRAS, 365, 1067
Dauser, T., Garcia, J., Parker, M. L., Fabian, A. C., & Wilms, J. 2014, MNRAS, 444, L100
de Rosa, A., Bassani, L., Ubertini, P., Panessa, F., et al. 2008, A&A, 483, 749
Dehghanian, M., Ferland, G. J., Kriss, G. A., et al. 2019, ApJ, 877, 119
Done, C. 2010, arXiv:1008.2287
Done, C., Davis, S. W., Jin, C., Blaes, O., & Ward, M. 2012, MNRAS, 420, 1848
Drake, A. J., Djorgovski, S. G., Mahabal, A., et al. 2009, ApJ, 696, 870
Fabian, A. C., Alston, W. N., Cackett, E. M., et al. 2017, AN, 338, 269
Fabian, A. C., Kara, E., Walton, D. J., et al. 2013, MNRAS, 429, 2917
Fan, L. L., Wang, H. Y., Wang, T., et al. 2009, ApJ, 690, 1006
Freeman, P. E., Kashyap, V., Rosner, R., & Lamb, D. Q. 2002, ApJS, 138, 185
Gallagher, S. C., Brandt, W. N., Chartas, G., et al. 2006, ApJ, 644, 709
Gallagher, S. C., Brandt, W. N., Chartas, G., & Garmire, G. P. 2002, ApJ, 567, 37
Gandhi, P., Lansbury, G. B., Alexander, D. M., et al. 2014, ApJ, 792, 117
García, J., Dauser, T., Lohfink, A., et al. 2014, ApJ, 782, 76
Gehrels, N. 1986, ApJ, 303, 336
George, I. M., & Fabian, A. C. 1991, MNRAS, 249, 352
George, I. M., Turner, T. J., Netzer, H., et al. 1998, ApJS, 114, 73
Gibson, R. R., Jiang, L., Brandt, W. N., et al. 2009, ApJ, 692, 758
Gierliński, M., & Done, C. 2004, MNRAS, 349, L7
Gilfanov, M., & Merloni, A. 2014, SSRv, 183, 121
Giustini, M., & Proga, D. 2019, A&A, 630, A94
Gupta, K. K., Ricci, C., Tortosa, A., et al. 2021, MNRAS, 504, 428
HI4PI Collaboration, Ben Bekhti, N., Flöer, L., et al. 2016, A&A, 594, A116
Hickox, R. C., & Alexander, D. M. 2018, ARA&A, 56, 625
Huang, J., Luo, B., Du, P., et al. 2020, ApJ, 895, 114
Immler, S., Brandt, W. N., Vignali, C., et al. 2003, AJ, 126, 153
Jiang, Y.-F., Stone, J. M., & Davis, S. W. 2014, ApJ, 796, 106
Jiang, Y.-F., Stone, J. M., & Davis, S. W. 2019, ApJ, 880, 67
Just, D. W., Brandt, W. N., Shemmer, O., et al. 2007, ApJ, 665, 1004
Kaastra, J. S., Kriss, G. A., Cappi, M., et al. 2014, Sci, 345, 64
Kraft, R. P., Burrows, D. N., & Nousek, J. A. 1991, ApJ, 374, 344
Krawczyk, C. M., Richards, G. T., Mehta, S. S., et al. 2013, ApJS, 206, 4
Laha, S., Reynolds, C. S., Reeves, J., et al. 2021, NatAs, 5, 13
Lansbury, G. B., Stern, D., Aird, J., et al. 2017, ApJ, 836, 99
Laurenti, M., Piconcelli, E., Zappacosta, L., et al. 2022, A&A, 657, A57
Leighly, K. M., Halpern, J. P., Jenkins, E. B., et al. 2007a, ApJ, 663, 103
Leighly, K. M., Halpern, J. P., Jenkins, E. B., & Casebeer, D. 2007b, ApJS, 173, 1
Leighly, K. M., Terndrup, D. M., Lucy, A. B., et al. 2019, ApJ, 879, 27
Liu, H., Luo, B., Brandt, W. N., et al. 2019, ApJ, 878, 79
Liu, H., Luo, B., Brandt, W. N., et al. 2021, ApJ, 910, 103
Liu, H., Luo, B., Brandt, W. N., Gallagher, S. C., & Garmire, G. P. 2018, ApJ, 859, 113
Longinotti, A. L., Kriss, G., Krongold, Y., et al. 2019, ApJ, 875, 150
Luo, B., Brandt, W. N., Alexander, D. M., et al. 2013, ApJ, 772, 153
Luo, B., Brandt, W. N., Alexander, D. M., et al. 2014, ApJ, 794, 70
Luo, B., Brandt, W. N., Hall, P. B., et al. 2015, ApJ, 805, 122
Lusso, E., & Risaliti, G. 2017, A&A, 602, A79
Lutz, D., Maiolino, R., Spoon, H. W. W., & Moorwood, A. F. M. 2004, A&A, 418, 465
Madsen, K. K., Burwitz, V., Forster, K., et al. 2021, arXiv:2111.01613
Mainzer, A., Bauer, J., Cutri, R. M., et al. 2014, ApJ, 792, 30
Marconi, A., Axon, D. J., Maiolino, R., et al. 2008, ApJ, 678, 693
Marconi, A., Axon, D. J., Maiolino, R., et al. 2009, ApJL, 698, L103
Martin, D. C., Fanson, J., Schiminovich, D., et al. 2005, ApJL, 619, L1
Martocchia, S., Piconcelli, E., Zappacosta, L., et al. 2017, A&A, 608, A51
Mateos, S., Carrera, F. J., Alonso-Herrero, A., et al. 2015, MNRAS, 449, 1422
Matthews, J. H., Knigge, C., Long, K. S., et al. 2016, MNRAS, 458, 293
Mehdipour, M., Kaastra, J. S., Kriss, G. A., et al. 2017, A&A, 607, A28
Mehdipour, M., Kriss, G. A., Kaastra, J. S., et al. 2021, A&A, 652, A150
Mineshige, S., Kawaguchi, T., Takeuchi, M., & Hayashida, K. 2000, PASJ, 52, 499
Miniutti, G., Brandt, W. N., Schneider, D. P., et al. 2012, MNRAS, 425, 1718
Murray, N., Chiang, J., Grossman, S. A., & Voit, G. M. 1995, ApJ, 451, 498
Nandra, K., Barret, D., Barcons, X., et al. 2013, arXiv:1306.2307
Nardini, E., Lusso, E., Risaliti, G., et al. 2019, A&A, 632, A109
Netzer, H. 1993, ApJ, 411, 594
Netzer, H. 2015, ARA&A, 53, 365
Netzer, H., & Marziani, P. 2010, ApJ, 724, 318
Neugebauer, G., Green, R. F., Matthews, K., et al. 1987, ApJS, 63, 615
Ni, Q., Brandt, W. N., Luo, B., et al. 2018, MNRAS, 480, 5184
Ni, Q., Brandt, W. N., Luo, B., et al. 2022, MNRAS, 511, 5251
Ni, Q., Brandt, W. N., Yi, W., et al. 2020, ApJL, 889, L37
O'Donnell, J. E. 1994, ApJ, 422, 158
Ohsuga, K., & Mineshige, S. 2011, ApJ, 736, 2
Panagiotou, C., & Walter, R. 2019, A&A, 626, A40
Park, T., Kashyap, V. L., Siemiginowska, A., et al. 2006, ApJ, 652, 610
Planck Collaboration, Aghanim, N., Akrami, Y., et al. 2020, A&A, 641, A6
Proga, D., Stone, J. M., & Kallman, T. R. 2000, ApJ, 543, 686
Pu, X., Luo, B., Brandt, W. N., et al. 2020, ApJ, 900, 141
Reeves, J. N., Turner, M. J. L., Ohashi, T., & Kii, T. 1997, MNRAS, 292, 468

Ricci, C., Loewenstein, M., Kara, E., et al. 2021, ApJS, 255, 7
Ricci, C., Trakhtenbrot, B., Koss, M. J., et al. 2017, ApJS, 233, 17
Ricci, C., Walter, R., Courvoisier, T. J. L., & Paltani, S. 2011, A&A, 532, A102
Ross, R. R., & Fabian, A. C. 2005, MNRAS, 358, 211
Rovilos, E., Georgantopoulos, I., Akylas, A., et al. 2014, MNRAS, 438, 494
Sabra, B. M., & Hamann, F. 2001, ApJ, 563, 555
Saez, C., Brandt, W. N., Gallagher, S. C., Bauer, F. E., & Garmire, G. P. 2012, ApJ, 759, 42
Schartel, N., Rodríguez-Pascual, P. M., Santos-Lleó, M., et al. 2005, A&A, 433, 455
Scott, A. E., Stewart, G. C., Mateos, S., et al. 2011, MNRAS, 417, 992
Shemmer, O., Brandt, W. N., Netzer, H., Maiolino, R., & Kaspi, S. 2008, ApJ, 682, 81
Shen, Y., & Ho, L. C. 2014, Natur, 513, 210
Shen, Y., Richards, G. T., Strauss, M. A., et al. 2011, ApJS, 194, 45
Skrutskie, M. F., Cutri, R. M., Stiening, R., et al. 2006, AJ, 131, 1163
Steffen, A. T., Strateva, I., Brandt, W. N., et al. 2006, AJ, 131, 2826
Stern, D. 2015, ApJ, 807, 129
Strateva, I. V., Brandt, W. N., Schneider, D. P., Vanden Berk, D. G., & Vignali, C. 2005, AJ, 130, 387
Sulentic, J. W., Zwitter, T., Marziani, P., & Dultzin-Hacyan, D. 2000, ApJL, 536, L5
Takeuchi, S., Ohsuga, K., & Mineshige, S. 2014, PASJ, 66, 48
Tananbaum, H., Avni, Y., Branduardi, G., et al. 1979, ApJL, 234, L9
Teng, S. H., Brandt, W. N., Harrison, F. A., et al. 2014, ApJ, 785, 19
Trakhtenbrot, B., Arcavi, I., MacLeod, C. L., et al. 2019, ApJ, 883, 94
Turner, T. J., George, I. M., Nandra, K., & Mushotzky, R. F. 1997, ApJS, 113, 23
Turner, T. J., & Miller, L. 2009, A&ARv, 17, 47
Ueda, Y., Eguchi, S., Terashima, Y., et al. 2007, PThPS, 169, 295
Vanden Berk, D. E., Richards, G. T., Bauer, A., et al. 2001, AJ, 122, 549
Veilleux, S., Rupke, D. S. N., Kim, D. C., et al. 2009, ApJS, 182, 628
Wang, J.-M., & Netzer, H. 2003, A&A, 398, 927
Wills, B. J., Shang, Z., & Yuan, J. M. 2000, NewAR, 44, 511
Winter, L. M., Mushotzky, R. F., Reynolds, C. S., & Tueller, J. 2009, ApJ, 690, 1322
Wright, E. L., Eisenhardt, P. R. M., Mainzer, A. K., et al. 2010, AJ, 140, 1868
Yamada, S., Ueda, Y., Tanimoto, A., et al. 2020, ApJ, 897, 107
Yi, W., Brandt, W. N., Ni, Q., et al. 2022, ApJ, 930, 5
York, D. G., Adelman, J., Anderson, J. E. J., et al. 2000, AJ, 120, 1579
Yuan, M. J., & Wills, B. J. 2003, ApJL, 593, L11